Application of an epidemic spreading model to characterize amyloid beta accumulation in familial Alzheimer's disease mutation carriers

ELIZABETH LEVITIS
Integrated Program in Neuroscience
McGill University, Montreal
March 2020

A thesis submitted to McGill University in partial fulfillment of the requirements of the degree of Masters of Science

Abstract

Previous work has shown that the spatial pattern of amyloid beta (Aβ) deposition in individuals spanning the sporadic Alzheimer's disease (AD) spectrum can be reproduced with high accuracy using an epidemic spreading model (ESM), which simulates the diffusion of Aβ across neuronal connections and is constrained by individual rates of Aβ production and clearance. As a biologically constrained model, the ESM can provide insight into the mechanisms underlying Aβ spread and can help clarify where Aβ begins to accumulate earliest in the disease process.

While sporadic AD accounts for the bulk of AD cases, AD can also arise as a result of one of three distinct autosomal dominant mutations, all of which result in an abnormal amount of Aβ. The primary objective of this thesis is to shed light on whether the spatial pattern of Aβ in individuals with familial form of AD (fAD) can also be explained using the ESM, and we split this work into two main parts. First, we explore whether baseline patterns of Aβ can be reproduced with comparable accuracy to what was reported for sAD. Recent work has suggested that the methodological choices made regarding reference region and intensity normalization in PET processing substantially influence Aβ measurements, and we subsequently compared results across multiple PET processing pipelines, measures of connectivity, and potential epicenters. We found that as with sAD, the most likely epicenters of Aβ spread are cortical regions that are part of the default mode network. The top two models explained 35% and 44% of the group-level variance in regional Aβ levels (n=249).

Our second aim was to evaluate the utility of ESM in a longitudinal context for prediction of regional Aβ accumulation within-subject. In this experiment, we applied the ESM within-subject to learn the relationship, or set of subject-specific ESM parameters, between two initial timepoints, and we extrapolated this relationship to predict Aβ patterns of 44 MC who had a third visit. This objective proved difficult, likely due in part to the underlying heterogeneity in change across time and the potential noise in our longitudinal measurements. Overall, we were able to explain on average 11% of the variance in the observed rates of regional Aβ change, and the performance was highest for subjects who had consistent rates of change between visits.

Future improvements to the modelling of regional Aβ accumulation may include improved measurement of Aβ, incorporation of group-level information and the epicenters gleaned from the cross-sectional ESM application.

Résumé

Des travaux antérieurs ont montré que la distribution spatiale de dépôts amyloïde chez les individus atteints de la forme liée à l'âge de la maladie d'Alzheimer (MA) peut être reproduite avec grande précision au moyen d'un modèle de propagation épidémique. Ce modèle simule la diffusion d'amyloïde à travers les réseaux de neurones et est contraint par les taux individuels de production et de clairance de la protéine. Du fait de ses contraintes biologiques, le modèle de propagation épidémique fournit un aperçu des mécanismes sous-jacents à la propagation de la bêta-amyloïde et aide à identifier les cibles précoces d'accumulation de cette protéine au cours de la maladie.

Bien que la forme liée à l'âge constitue la majorité des cas, la MA peut également survenir à la suite de l'une de trois mutations autosomiques dominantes distinctes, toutes résultant en une quantité anormale de bêta-amyloïde. L'objectif principal de cette thèse est de donner une explication plausible, au moyen du modèle de propagation épidémique, de la distribution spatiale de dépôts amyloïde chez les individus atteints de formes familiales héréditaires de la MA. Ce travail se fera en deux temps. Nous allons d'abord examiner si la distribution spatiale de référence de l'amyloïde peut être reproduite avec une précision comparable à celle observée pour la MA liée à l'âge (r2 = 46%). Des travaux récents suggèrent que les choix méthodologiques concernant la région de référence et la normalisation d'intensité dans le pré-traitement des données de tomographie par émission de positons (TEP) influencent de manière importante les mesures de bêta-amyloïde. Nous comparons ensuite les résultats provenant de plusieurs chaînes de traitement en TEP, les mesures de connectivité et les épicentres potentiels. Nos résultats montrent que tout comme dans la forme liée à l'âge, les cibles les plus probables de propagation de l'amyloïde sont les régions corticales faisant partie du réseau du mode par défaut. Les deux modèles principaux expliquent 35% et 44% de la variance des niveaux régionaux de bêta-amyloïde au niveau du groupe (n = 249).

Notre deuxième objectif était d'évaluer le modèle de propagation épidémique dans un contexte longitudinal pour la prédiction d'accumulation régionale de bêta-amyloïde intra-sujet. Au cours de cette expérience, nous avons appliqué le modèle de propagation épidémique pour étudier la relation, ou les paramètres du modèle spécifiques au sujet, entre deux points initiaux dans le temps et nous avons extrapolé cette relation pour prédire la distribution de bêta-amyloïde de 44 porteurs de mutation ayant eu trois visites. Cet objectif s'avéra difficile, peut-être dû en partie à

l'hétérogénéité sous-jacente des changements dans le temps et du bruit dans nos mesures longitudinales. Nous avons en moyenne pu expliquer 11% de la variance dans les changements de taux de bêta-amyloïde observés et la performance était plus élevée pour les sujets ayant des taux de variation consistants entre les visites.

Des améliorations à la modélisation de l'accumulation régionale de bêta-amyloïde pourraient inclure une meilleure mesure de bêta-amyloïde, l'intégration d'information au niveau du groupe et des épicentres estimés à partir de l'application transversale du modèle de propagation épidémique.

Contents

List of Figures

List of Tables

List of Abbreviations

Aβ	**A**myloid β
AD	**A**lzheimer's **D**isease
ADNI	**A**lzheimer's **D**isease **N**euroimaging **I**nitiative
aMCI	**a**mnestic **M**ild **C**ognitive **I**mpairment
APOE	**APO**lipoprotein **E**
APP	**A**myloid **P**recursor **P**rotein
APPIAN	**A**utomated **P**ipeline for **P**ET **I**mage **AN**alysis
CN	**C**ognitively **N**ormal
DIAN	**D**ominantly **I**nherited **A**lzheimer's **N**etwork
DMN	**D**efault **M**ode **N**etwork
ESM	**E**pidemic **S**preading **M**odel
fAD	**f**amilial **A**lzheimer's **D**isease
fMRI	**f**unctional **M**agnetic **R**esonance **I**maging
MCI	**M**ild **C**ognitive **I**mpairment
MRI	**M**agnetic **R**esonance **I**maging
PET	**P**ositron **E**mission **T**omography
PSEN1	**P**re**SEN**ilin **1**
PSEN2	**P**re**SEN**ilin **2**
PUP	**P**ET **U**nified **P**ipeline

Acknowledgements

I would like to first and foremost thank Dr. Alan C. Evans for giving me the opportunity to join the McGill Center for Integrative Neuroscience as a software developer for the LORIS project and subsequently as a graduate student, where I have had the chance to surround myself with brilliant minds and supportive colleagues over the last three years. A huge thank you goes out to my co-supervisor, Dr. Yasser Iturria-Medina, for allowing me to carry out this project and providing me with guidance, support, and insight about academia and professional pursuits. Thank you to both of you for this incredible learning experience. Thank you to Dr. Bratislav Misic and Dr. Alain Dagher for being part of my supervisory committee and for the insightful discussions we have had about my project and the broader topics of network neuroscience and neurodegenerative disease modelling.

I'd like to thank so many of my colleagues within MCIN and the Montreal Neurological Institute. Firstly, I would like to thank Jake Vogel for taking me under his wing and being so patient with me as I immersed myself in the world of neuroimaging, Alzheimer's disease research, and computational disease progression modelling. I would like to thank Thomas Funck for teaching me about the intricacies of PET imaging and for giving me the opportunity to test and contribute to APPIAN. I would like to thank all the other labmates I have befriended and learned from - Noor Al-Sharif, Carolina Makowski, Stefan Drakulic, Neha Bhutani, Claude LePage. Thank you to Patrick Bermudes and PJ Toussaint for offering guidance to all the graduate students and for helping me translate my abtract (it's a shame I still haven't learned French).

I would like to thank Greg Kiar for his love and endless support, the countless hours we have spent working together (especially during the coronavirus quarantine), and for encouraging me to attain a better work-life balance. Thank you to all the friends I've had the pleasure of making outside of lab - special shoutout to Samantha Bovaird.

Last but not least, thank you to my parents, brother, and grandparents for their love and support throughout my journey at McGill University and for pushing me to always achieve my goals.

I have learned so much about neuroimaging and scientific rigor since joining MCIN, and I will forever look fondly upon my time here, where I found my niche at the intersection of neurological disease progression modelling, software development, and open science advocacy.

Declaration of Authorship

As the primary author of this thesis, I took the lead in executing the experiments. This included study design, data preprocessing, quality control, statistical analysis, visualization and interpretation of results, and writing of this thesis. However, I received invaluable guidance and assistance from several members of the lab.

- Alan C. Evans: study design, interpretation of results, thesis revision
- Yasser Iturria-Medina: study design, statistical analysis, interpretation of results
- Jacob W. Vogel: PET and fMRI processing, interpretation of results, statistical analysis, visualization
- Thomas Funck: PET data processing
- Gregory Kiar: statistical analysis, visualization, high performance computing

All the code used for analysis is available at https://github.com/llevitis/DIAN_ESM_AmyloidBeta_Project.git.

Chapter 1

Introduction

1.1 General context

Alzheimer's Disease (AD) is the principal neurodegenerative cause of dementia in the elderly, and its increasing prevalence has resulted in a huge effort to develop therapies, none of which have been able to successfully reverse the effects of the disease. AD predominantly affects adults aged 65 and older, and as our population continues to live longer, the prevalence of AD is expected to keep growing. The cumulative cost of medical diagnosis, treatment, and long-term care for individuals afflicted by AD is projected to be $47.1 trillion USD by 2050 (Association, 2018). Developing a therapy for AD is urgent, but the complexity and heterogeneity of the disease have made this a difficult goal to achieve.

The sporadic form of AD - or Late Onset Alzheimer's Disease (LOAD) – accounts for approximately 95% of all cases. LOAD manifests in a complex way, and its pathogenesis includes: toxic soluble forms of oligomeric amyloid-β (Aβ), extracellular Aβ senile plaques composed of insoluble Aβ fibrils, intracellular neurofibrillary tangles composed of hyperphosphorylated tau protein, grey matter atrophy, and vascular dysregulation. Thus far there is no consensus on the exact pathophysiological cause(s) of LOAD, and this has hindered the development of successful therapies.

Two of the leading hypotheses for the cause of AD are the amyloid cascade hypothesis and the vascular dysregulation hypothesis. The former posits that the soluble Aβ oligomers are the cause of neurotoxicity and synaptoxicity while the latter posits that impaired blood flow substrate delivery and neuronal/glial energy demands are what cause brain dysfunction and the progression of AD (Karran, Mercken, and Strooper, 2011, Iadecola, 2013, Iadecola, 2004, Zlokovic, 2011). Recently, a data driven analysis of sporadic AD pointed to vascular dysregulation as one of the earliest pathological events driving AD progression (Iturria-Medina et al., 2016).

In tandem, a mechanistic epidemic spreading model was introduced that could reproduce cross-sectional spatiotemporal patterns of Aβ in individuals along the AD spectrum, and impaired Aβ clearance was the model parameter most significantly related to clinical diagnosis (Iturria-Medina et al., 2014). One possible explanation proposed for reduced clearance is a cerebrovascular dysfunction in the form of the blood-brain barrier (BBB) permeability breakdown. There is significant evidence corroborating the presence of vascular dysregulation in preclinical AD; however, age is a major confounding factor in the study of vascular dysregulation as a cause of AD development, and not just a non-pathological aging effect (Rius-Pérez et al., 2018). To address this, we turn to the Dominantly Inherited Alzheimer's Network, a study representative of the second form of AD, familial or early-onset autosomal dominant AD (ADAD). ADAD can arise in individuals with a pathogenic mutation in one of three genes, coding for amyloid precursor protein (APP), presenilin 1 (PSEN1), and presenelin 2 (PSEN2). In ADAD mutation carriers will invariably develop dementia.

1.2 Objectives

Aim 1: Cross-sectional
Assess whether the previously developed epidemic spreading model (ESM) can explain patterns of Aβ in the brains of ADAD mutation carriers. The overall goal was to determine whether the mechanisms spurring Aβ accumulation are shared by both forms of AD. We additionally assessed the robustness of the model to different image processing pipelines and measures of connectivity.
Aim 2: Longitudinal
Using longitudinal data, evaluate the reliability of within subject ESM parameters by assessing whether they can be used to predict future regional patterns of Aβ.

Chapter 2

Review of the Literature

2.1 Alzheimer's disease

To date, there is no cure for AD, the principle neurodenerative cause of dementia. Treating patients with dementia is costly - in 2009, the average cost for a patient with AD was roughly 57,000 USD (Burns and Iliffe, 2009). The socioeconomic gravity of treating AD has spurred research seeking to prevent or mitigate AD by developing early biomarkers (Shah et al., 2016).

The two main pathological signs of AD are neurofibrillary tau tangles and Aβ senile plaques, and both are required to definitely confirm AD at autopsy (McKhann et al., 2011). Aβ peptides are formed by the sequential cleavage of the APP by β-cleaving amyloid precursor enzyme (BACE) and gamma-secretase. The peptides vary in length from 40-42 residues, and earlier studies showed that these peptides are what comprise the primary structural component of insoluble fibrils accumulating in the Aβ senile plaques found in post-mortem brains of AD patients. Historically, these insoluble amyloid plaques were posited as being toxic to neuronal cells while monomeric soluble forms were deemed harmless (Walsh and Selkoe, 2007). However, the Aβ animal-model literature showed an increasing disconnect between plaque pathology and memory impairment; this was evidenced by several reports of cognitive deficits appearing before plaque deposition in transgenic mouse models of AD (Hsia et al., 1999, Mucke et al., 2000, Westerman et al., 2002). More recent research has identified an intermediate misfolded form of Aβ, soluble Aβ oligomers, as a potential driver of memory impairment (Klein, 2012).

Most hypothetical models of AD progression, such as the one in Fig 2.1a, have been rooted in the amyloid cascade hypothesis, which posits that excessive amounts of soluble Aβ cause a buildup of insoluble Aβ, disrupting synaptic function and accelerating tau hyperphosphorylation (Hardy, 2002). Ultimately, this causes synaptic

death and eventual dementia. However, the order proposed in this hypothetical model has been disputed recently with the development of a data-driven model seeking to index the order in which biomarkers begin to become pathological in AD. Intra-brain vascular dysregulation was pointed to as an earlier biomarker of AD than Aβ plaques and lower CSF Aβ levels (Iturria-Medina et al., 2016). This does not preclude the possibility of soluble Aβ being the cytotoxic agent but does implicate vascular dysregulation as a necessary prelude that leads to the buildup of soluble Aβ in cells and the eventual cytoxicity involving tau protein.

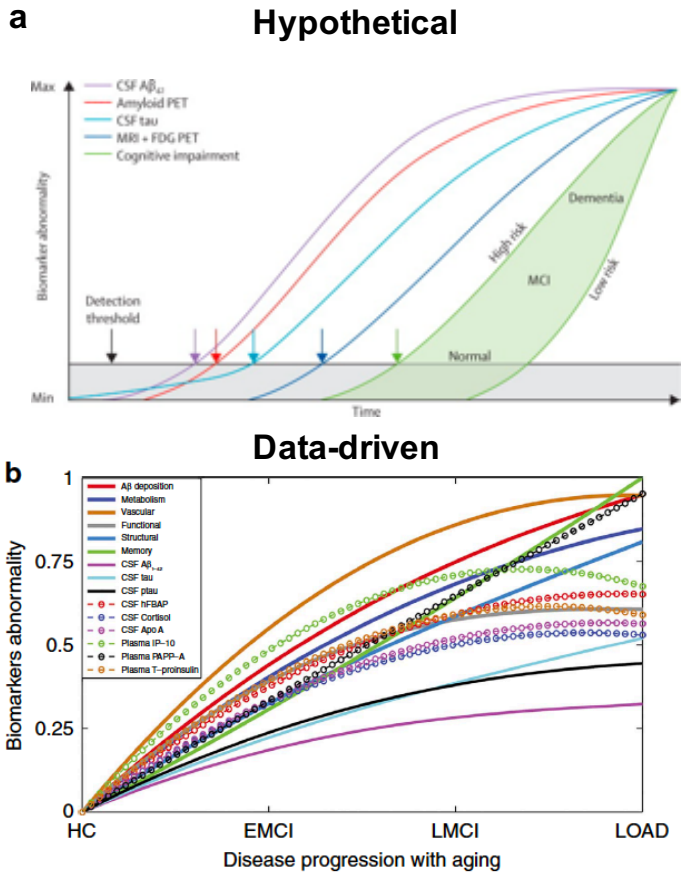

Figure 2.1: (a) Hypothetical model of AD progression, adapted from Jack et al, 2013. Changes in CSF and PET Aβ measurements come first, followed by changes in CSF tau increases, structural and metabolic changes, and finally cognitive impairment. (b) Data-driven model of AD progression, adapted from Iturria-Medina et al, 2016. Though Aβ changes occur early in the disease process, they are preceded by vascular changes.

2.1.1 Autosomal Dominant Alzheimer's Disease and Aβ as a core feature of AD

Most cases of AD are sporadic and are often referred to as late-onset as symptoms are exhibited later in life and have no definitive pathophysiologial cause. However,

1% of AD cases are genetic in nature and are caused by mutations in genes coding for three different proteins - Amyloid Precursor Protein (APP), Presenelin 1 (PSEN1), and Presenlin 2 (PSEN2). As the name suggests, APP is the precursor protein of many peptides including Aβ, and it is cleaved by PSEN1 and PSEN2, which are subunits of a larger catalytic complex (Haass, 2004). Mutations in all three genes have been shown to cause increased aggreggation of Aβ either by causing an overall increased production of Aβ peptides or increasing the production of a form of Aβ that aggreggates more easily (Haass et al., 2012). This finding has served as the foundation for the amyloid hypothesis, and the similar order of biomarker changes exhibited in individuals with sporadic AD (sAD) and familial AD (fAD) has lended support to the amyloid cascade hypothesis. However, as was described in the previous section, the involvement of Aβ in sporadic AD is much more complex, leading many to argue that these hypotheses are flawed. Nonetheless, an excellent review by Holtzmann and Musiek has enumerated a number of reasons for why Aβ is still of critical importance for sAD and fAD (Musiek and Holtzman, 2015). The greatest genetic risk factor contributing to sAD pathogenesis is APOE - specifically having at least one copy of the ApoE4 allele. ApoeE4 modulates AD pathology by promoting Aβ aggreggation and deposition into plaques, along with reduced Aβ clearance (Castellano et al., 2011, Fagan et al., 2002, Hudry et al., 2013, Vemuri et al., 2009, Verghese et al., 2013, Morris et al., 2010). In response to the poor correlation between Aβ load and decline in cognitive performance in sAD subjects, it is argued that, in both sAD and fAD, there is no anatomic colocalization of Aβ pathology and neurodegeneration. Furthermore, while tau pathology is much more anatomically colocalized with neurodegeneration, Aβ pathology appears to be required for spreading of tau pathology to neocortical areas in both sAD and fAD, and the presence of both Aβ and tau pathology is most strongly associated with cognitive decline, compared with either one or the other alone (Shepherd, McCann, and Halliday, 2009, Bateman et al., 2012, Price and Morris, 1999, Knopman et al., 2003, Tiraboschi et al., 2004).

Aβ is a key biomarker in both sAD and fAD, but where it shows up earliest may differ between the two. Unlike in sAD, where Aβ deposition is highest in neocortical areas, several groups have reported significantly increased striatal, thalamic, and neocortical Aβ deposition in fAD mutation carriers compared with noncarriers (Cohen et al., 2018, Gordon et al., 2018). One study evaluating differences between the PSEN1, PSEN2, and APP fAD mutation types found that all mutation types had high striatal PiB binding while some mutation carriers had higher cortical PiB binding. Interestingly, the PiB binding in the cortex was found to be lower in fAD mutation carrers than age-matched subjects with probable sAD (Villemagne et al., 2009). While the sample size of this study was small (n=30 fAD mutation carriers,

n=30 sAD subjects), the findings may suggest that the most probable area(s) of earliest Aβ accumulation may not be homogenous amongst all fAD mutation carriers.

Recently, an event-based model of disease progression was applied to fAD mutation carriers, and the authors found that the biomarker likeliest to exhibit the earliest deviation from normal levels was an aggreggate cortical Aβ deposition measure, followed by Aβ deposition in the caudate, putamen, accumbens, and thalamus (Oxtoby et al., 2018).

The therapeutic intervention strategies targeting Aβ fall into three main categories: reducing its production, promoting its clearance, and preventing its aggreggation into plaques. Determing which of these strategies is likeliest to be effective requires an understanding of the mechanisms via which soluble Aβ propogates and deposits in the brain and what is the ideal therapeutic window.

2.2 Modelling spatiotemporal trajectories of Aβ

Investigation into the formation of abnormal aggreggations of misfolded or conformational variants of the Aβ protein led to experimental evidence indicating that Aβ acts like a prion when misfolded. Specifically, cerebral β-amyloidosis, or the aggreggation of Aβ, can be induced in-vivo by exposure of APP-transgenic mice brains to dilute brain extracts containing aggreggated Aβ seeds (Kane et al., 2000, Walker et al., 2002, Meyer-Luehmann et al., 2006, Eisele et al., 2009, Watts et al., 2011). This gave rise to the prion-like hypothesis. It explains the progression of AD as being driven by the intercellular transfer of pathogenic proteins that propagate from initial host regions (Frost and Diamond, 2010, Frost, Jacks, and Diamond, 2009, Brundin, Melki, and Kopito, 2010). In the case of AD, the soluble Aβ oligomers are small and can easily be transferred either by absorption into axonal processes or by diffusion in the extracellular fluid (Nath et al., 2012, Hallbeck, Nath, and Marcusson, 2013, Song et al., 2014). Their spread between cells through the extracellular fluid is governed by principles of molecular diffusion, and as such, the sAβ transfer primarily occurs between anatomically interconnected areas or neighbouring neurons (Waters, 2010, Jucker and Walker, 2013, Walker and LeVine, 2012). Because the progression of AD, and other neurodegenerative disorders such as Parkinson's disease, are each linked to the misfolding of different proteins, the network degeneration hypothesis (NDH) has been proposed. The NDH posits that each disease is associated with its own anatomical pattern, and the hypothesis was corroborated by the correspondence between specific functional and anatomical covariance patterns and spatially distinguishable atrophy patterns of five different dementia syndromes (Palop, Chin, and Mucke, 2006, Seeley et al., 2009, Greicius et al., 2004, Buckner et al., 2005, Zhou et al.,

2012). In addition to addressing how sAβ spreads mechanistically, computational models developed to predict the macroscopic spread of Aβ must then recapitulate the spatiotemporal pattern of AD progression. Several models that attempt to do this have been developed in recent years, and in this section we will first introduce the neuroimaging methods used in this thesis followed by a comparison of the computational models.

2.2.1 Neuroimaging modalities and biomarkers of AD

Neuroimaging serves as a window into the brain, where different modalities allow us to quantify different structural or functional elements in the brain and ultimately validate computational models. The main elements we need to quantify are Aβ and connectivity strength between ROIs. For the former we use PET imaging whereas for the latter we can use either diffusion MRI or functional MRI.

2.2.1.1 PET

Although Aβ exists in both soluble and insoluble forms in the brain, we currently can only visualize the insoluble Aβ plaques using neuroimaging, specifically using Positron Emission Tomography (PET). PET uses a radioactive positron emitting isotope (a radionuclide) either alone or in combination with a larger molecule (a radiotracer). Different radiotracers bind to different metabolites either in the brain or body, allowing many different physiological processes to be measured in vivo. Several radiotracers currently exist which bind to fibrillar Aβ plaques - e.g. Florbetapir, the Pittsburgh Compound (PiB), Flumetamol - and they are injected intravenously. These radiotracers have different properties related to their half-life, specificity, and differing white and grey matter retention characteristics (Landau et al., 2014).

In the present study, the PET data was collected using several different protocols, with one difference being when subjects are put in a PET scanner following radiotracer injection. Dynamic PET scans are acquired from the time of radiotracer injection and allow us to quantify the long-term behavior of a radiotracer in the tissue. Static PET scans are acquired after the radiotracer has reached steady state in the body, and pharmacokinetic information is thus lost, resulting in less precise final quantification (K., 2013). As will be presented in Chapter 3.5, there are several choices that can be made when processing PET data to quantify radiotracer binding, but firstly, a PET scan is typically co-registered - or aligned - to an individual's structural MRI (sMRI) scan which has much greater spatial resolution and anatomical detail. Poor PET resolution results in "partial volume effects" (PVE), wherein multiple tissue types - grey matter, white matter, and CSF - can contribute to the PET signal from

a given voxel, leading to either over- or under- estimation of signal in that voxel. This issue can be addressed using various partial volume correction (PVC) methods, and for this study we use the gold standard, the geometric transfer matrix method (Meltzer et al., 1990, GTM: Rousset, Ma, and Evans, 1998). Following optional PVC, the PET signal can be regionally quantified. In most AD PET studies, the quantification method used is the standard uptake value ratio (SUVR) applied to statically acquired scans, where the signal in every voxel is divided by the average signal in a region that is considered to be devoid of any specific radiotracer binding (Lopresti et al., 2005).

Unlike statically acquired PET scans, dynamically acquired scans are the only ones that allow for a fully quantitative measurement of radiotracer binding. The volume of distribution (V_T) of a radiotracer is defined as the the ratio of the radiotracer concentration in an ROI (C_T) to the radiotracer concentration in plasma (C_P) at equilibrium. As with the SUVR method, when a reference region is available, the V_T^{ref} can be computed for a reference region. The Logan plot method, a compartment modelling technique that uses linear regression, can be used to estimate the V_T and V_T^{ref} over the timecourse of a PET scan (Logan et al., 1990). The binding potential of a radiotracer, i.e. the density of available receptors for a specific radiotracer, is is computed using Equation 2.1, and the distribution volume ratio (DVR) is equivalent to $BP_{ND} + 1$.

$$BP_{ND} = (V_T / V_T^{ref}) - 1 \tag{2.1}$$

$$DVR = V_T / V_T^{ref} \tag{2.2}$$

PET Aβ scans that have been normalized using the Logan Plot method with respect to the cerebellar gray matter reveal individuals who are cognitively normal typically have little to no Aβ presence in the brain and that the presence of Aβ is variable in mild cognitively impaired individuals (Fig 2.2, Mathis, Lopresti, and Klunk, 2007). In patients with greater cognitive deficit we typically observe higher levels of Aβ in areas such as the precuneus and medial orbitofrontal cortex. However, it is important to note that this correlation is not absolute. Subjects who are cognitive normal may have high Aβ levels while the opposite is also found, and different proportions of amyloid-positive cognitively normal older patients have been reported, most frequently ranging from 10-30% (Chételat et al., 2013).

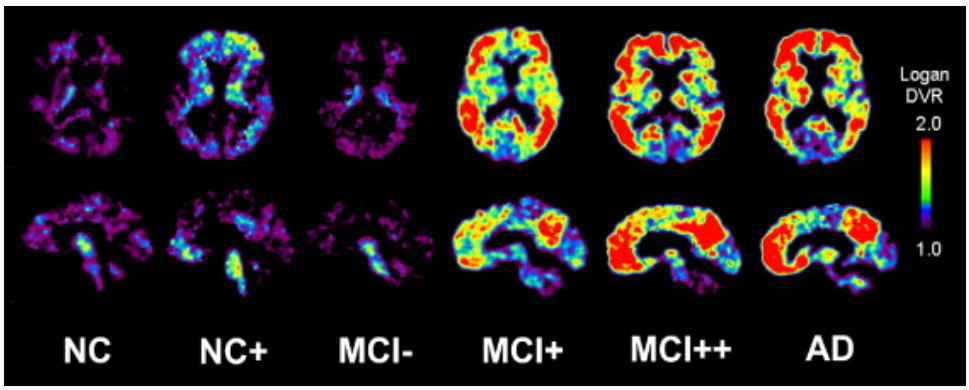

Figure 2.2: From left to right, we see individuals who have varying levels of PiB binding across the AD spectrum. CN = Cognitively Normal; Reproduced from Mathis, Lopresti, and Klunk, 2007

2.2.1.2 MRI

Broadly speaking, the brain is comprised of grey matter, white matter, and CSF. The grey matter is where cell bodies of neurons are located whereas the white matter consists of a high density of myelinated axons, the connective tissue of the brain. Different MRI techniques all use an external magnetic field to manipulate the magnetic relaxation properties of white and grey matter to produce different types of contrast such that we can learn more about the underlying structure or function of the brain (Pooley, 2005). Here we use T1-weighted sMRI, resting-state functional MRI (rsfMRI), and diffusion tensor imaging (DTI).

T1-weighted structural MRI scans have contrast based on the longitudinal relaxation of tissue, and they provide superior spatial resolution such that we can discern the different tissue types from one another most clearly. For this thesis we only use sMRI to identify anatomical regions of interest, as well as grey matter volume and cortical thickness. These measures can be used to assess whether there has been cortical atrophy or neurodegeneration, a phenomenon that occurs in the later stages of AD.

Water molecules travel differently in distinct tissue types, and diffusion MRI leverages this difference to create contrast. DTI scans are 4D scans where the 4th dimension is the number of possible diffusion directions of the water molecules. Each voxel in the scan contains information about a specific direction of diffusion and the rate of diffusion along that axis. The primary direction of diffusion of water is most highly correlated with the principle axis of a myelinated axon. As a result, DTI scans convey the most information about white matter pathways connecting different regions of the brain. To generate a connectivity matrix, DTI scans need to be pre-processed, registered to either a subject's T1-weighted MRI scan or a stereotaxic template, traced, and segmented into a graph (Soares et al., 2013).

Functional MRI measures blood flow in the brain as a proxy for neuronal activity. When neurons are active, oxygenated blood rushes towards areas of activity to replenish the depleted resources. A localized increase in oxygenated blood is thus reflected as a localized increase in fMRI signal. As the name suggests, rsfMRI scans are acquired while a subject is at rest, and the synchronized signal between regions can be used to infer which regions are correlated and exhibit a "functional connectivity". As with DTI, fMRI is used to create a template functional connectivity matrix. The patient's sMRI scan is spatially normalized such that the brains of all subjects are in the same 3D "stereotaxic" space, and rsfMRI scans are co-registered to the sMRI scans. A number of preprocessing steps must be taken to account for potential artifacts arising from but not limited to physiological activity, motion, white matter and ventricle signal, and low signal to noise ratio. The preprocessed rsfMRI scans are parcellated with the ROIs drawn from the sMRI data, and the time-series of the ROIs are correlated to generate correlation matrices. A combination of confounds can be regressed out prior to the correlation matrices being averaged to create a template functional connectivity matrix.

2.2.2 Network Diffusion Model

The first computational model seeking to reproduce the macroscopic spatiotemporal spread of misfolded proteins is the Network Diffusion Model (NDM, Raj, Kuceyeski, and Weiner, 2012). In keeping with the NDH, the NDM sought to predict spatially dissociable "persistent modes" of disease spread for two types of dementia, AD and the behavioral variant of frontotemporal dementia (bvFTD). Cortical atrophy quantified using voxelwise morphometry was used as a proxy of misfolded protein presence. The spread of AD pathology was modelled as a diffusive process across an anatomical brain network whose nodes represent cortical or subcortical grey matter structures and whose edges represent white matter fiber pathways connecting the structures. The overall brain-wide hypothesized atrophy was taken as the sum of the atrophy patterns contributed by individual eigenmodes, i.e. the eigenvectors corresponding to specific sets of brain regions that explain the most variance in the data. The authors found that the eigenmodes corresponded to brain regions known to be implicated in AD and bvFTD, reaffirming the NDH. The same team subsequently applied the NDM to the Alzheimer's Disease Neuroimaging Initiative (ADNI) dataset, and they were able to capture future changes in regional atrophy and metabolic states with a correlation of 90% to 96% across clinical diagnoses. (Raj et al., 2015).

2.2.3 Epidemic Spreading Model

The NDM did not actually reproduce the propagation of misfolded proteins (MP). Seeking to address the limitations of the NDM, an Epidemic Spreading Model (ESM) of AD was developed to stochastically reproduce Aβ propagation and deposition. Unlke the NDM which only accounts for misfolded proteins being deposited by macroscopic regions, the ESM allows for an ROI to be endogenously or exogenously infected and, importantly, for misfolded proteins to be cleared from a region. The overarching non-linear differential equation of the model posits that the change in MP deposition in an ROI is equal to the probability of endogenously producing and exogenously receiving MP from connected ROIs minus the probability of clearing the deposited MP. A more thorough explanation of the mathematical modelling is provided in Chapter 3.4.

When applied to over 700 subjects in the ADNI dataset, the ESM was able to explain 46-57% of the variance in the mean regional Aβ deposition probabilities of the distinct subgroups and identified starting seed regions for Aβ propagation, the posterior and anterior cingulate cortices. These seed regions are in agreement with what has been established in the literature (Palmqvist et al., 2017). To compare the NDM and ESM, the authors implemented the NDM for the same dataset and found that the NDM was able to explain 27-33% of the variance in the mean regional SUVR values of the distinct subgroups and identified the same starting seed regions for Aβ propagation.

Perhaps the most interesting findings from the ESM analysis was the significant association between individuals' Aβ clearance rates and their clinical diagnosis. As a clinical predictor, the clearance rate did significantly better than the Aβ production rate. Aβ can be cleared a number of ways, many of which are mediated by glial cells. In brief - glial cells can produce proteases that hydrolyze Aβ at different cleavage sites, release extracellular chaperones that facilitate the exit of Aβ across the blood brain barrier (BBB), either independently or in association with receptors/transporters, or by phagocytosis of Aβ in the case of astrocytes and microglia (Ries and Sastre, 2016). As was mentioned previously, reduced clearance could be driven by vascular dysregulation that may in fact precede a build-up of toxic soluble Aβ in the brain.

One aim of this thesis is to apply the ESM to baseline PiB-PET data of fAD mutation carriers to assess whether the regional pattern of Aβ can in fact be reproduced using the ESM and to compare mechanistic differences between fAD and sAD using the ESM model parameters.

2.2.4 Time-Varying Accumulation, Clearance, and Propagation Model

As had been pointed out with the introduction of ESM, one drawback of NDM is that the underlying differential equations in NDM assume a constant rate of change in MP behaviour, and a diffusion model may accurately capture MP propagation dynamics over the short term but not over the long-term disease timecourse. An Accumulation, Clearance, and Propagation (ACP) model has been introduced recently which addresses this issue by modelling MP progression with a Gaussian process (GP), where short term changes in MP concentration in a given ROI are used to estimate group-level long-term trajectories, and the dynamics of overall MP progression are constrained by a non-linear differential equation that considers biologically feasible dynamics of MP accumulation, clearance, and propagation much like the ESM does (Garbarino, Lorenzi, and for the Alzheimer's Disease Neuroimaging Initiative, 2019). Briefly, a GP is a probability distribution over possible functions that can describe some set of observations. With more observations, Bayesian inference can be used to narrow iteratively the distribution of possible functions such that predictions about future observations can be made more accurately. Using this methodology, the authors were able to fit long-term trajectories of ROI accumulation in a set of 11 macroscopic ROIs using longitudinal observations from the ADNI cohort.

While the ESM is fit individually for each subject and only uses group-level model fit to infer probable epicenters of MP spread, the ACP makes use of longitudinal observations across all subjects to obtain a set of group-level model parameters that also vary with time. The ACP is ultimately able to reconstruct within ROI long-term trajectories more accurately than a simpler diffusion model, and when applied to unseen data of individual subjects, the mean RMSE across the 11 ROIs ranges from 0.11-0.21.

One drawback of the ACP is that it assumes that everyone follows the same disease progression pattern. Several recent data-driven models have shown that alterations in distinct biomarkers including Aβ do not occur uniformly across individuals (Iturria-Medina, Carbonell, and Evans, 2018). In particular, one such model, Subtype and Stage Inference (SuStain), has been applied to volumetric MRI data from the ADNI cohort to show that the phenotypic heterogeneity observed between individuals can be mapped to three distinct subtypes (Young et al., 2018).

For Aim 2, we assess whether fitting the ESM within subject between two visits - without incorporation of group-level information, as in ACP - allows us to accurately predict future regional patterns of Aβ.

Chapter 3

Materials and methods

3.1 Participants

Participants of this study represented a selection of individuals from one multi-center study, the Dominantly Inherited Alzheimer's Network (DIAN; https://dian.wustl.edu). The DIAN dataset is comprised of individuals from families known to have mutations in the presenilin 1 (PSEN1), presenilin 2 (PSEN2). Both mutation carriers and non-carriers were used for different stages of the analysis, and we used all individuals from the 12th semiannual DIAN datafreeze who passed imaging quality control and had at least one PiB PET scan. In total, 215 mutation carriers were included for the baseline analysis. For the longitudinal analysis, 115 mutation carriers had two scans available, and 34 of them had a third scan available. Dementia status was determined using the clinical dementia rating (CDR), and mutation status was determined Bateman et al., 2012. The CDR is a five point scale ranging from 0-3: no dementia (CDR=0), very mild dementia (CDR=0.5), mild cognitive impairment (CDR=1), moderate cognitive impairment (CDR=2), and severe dementia (CDR=3). Demographic information can be found in Table 3.1. Estimated years to symptom onset (EYO) are calculated as the age of the participant minus the age of their parent when the parent began to exhibit symptoms. Thus, negative EYO indicates that a participant was scanned before symptom onset.

Table 3.1: Demographic information.

	1st Timepoint	2nd Timepoint	3rd Timepoint	
N (Mutation Carriers)	215	121	44	
N (Noncarriers)	0	72	10	
Age (SD)	39.01 (10.68)	42.12 (9.71)	46.8 (7.98)	
% Women	56.28%	60.1%	61.36%	EYO
Education (SD)	14.26 (2.88)	14.44 (2.66)	13.98 (2.31)	
EYO (SD)	-7.28 (10.98)	-4.7(9.83)	2.15 (4.84)	
% ApoE4	28.84%	29.53%	43.18%	
PET Reference Region	CC/Brainstem	Brainstem	Brainstem	

= estimated years to symptom onset; AD = Alzheimer's disease dementia, SD = Standard Deviation

3.2 Structural MRI and quality control

Whole-brain T1-weighted MPRAGE images (TR = 2300 ms, TE = 2.95 ms, flip angle = 9) with 1.1 mm x 1.1 mm x 1.2 mm voxel size were acquired. In addition to performing manual QC, we tested the generalizability of MRIQC, an automatic MRI quality control tool that generates image quality metrics (IQMs) related to noise, information theory, and specific artifacts (Esteban et al., 2017). Subsequently, we ran MRIQC's built-in Random Forrest Classifier to predict whether a scan should be rejected or used for further analysis based on its associated IQMs. Manual QC was found to be necessary to validate MRIQC's predictions to determine whether scans were failed by MRIQC due to atrophy or actual motion artifacts. Scans that were failed due to atrophy were kept.

3.3 PET Acquisition and Pre-processing

Aβ imaging was performed with a bolus injection of 15 mCi of [11C]PiB. Scans were either acquired dynamically, starting at injection for 70 minutes, or statically, starting at 40 minutes post-injection for 30 minutes. For analysis, only the PiB data between 40-70 minutes were used.

To assess how sensitive modelling is to preprocessing choices, we used two different pipelines to preprocess PET scans. The first of these was the PET Unified Pipeline (PUP; https://github.com/ysu001/PUP) (Su et al., 2013), and the second was the Automated Pipeline for PET Imaging Analysis (APPIAN; https://github.com/APPIAN-PET/APPIAN.git) (Funck et al., 2018).

With PUP, the processing steps used include smoothing, inter-frame motion correction and co-registration. Specifically, PET images in the 4dfp format are smoothed to achieve a common spatial resolution of 8mm to minimize inter-scanner differences

(Joshi et al., 2009). For scans that are dynamic, inter-frame motion correction is performed using standard image registration techniques (Hajnal et al., 1995) (Eisenstein et al., 2012). PET-MR registration is performed using a vector-gradient algorithm (VGM) (Rowland et al., 2005).

Prior to performing PET processing, APPIAN does structural preprocessing of T1 scans by coregistering the T1 MR image to stereotaxic space, which by default is the ICBM 152 6th generation non-linear brain atlas (Mazziotta et al., 2001). Coregistration is performed using an iterative implementation of minctracc (Collins et al., 1994 Mar-Apr). Brain tissue extraction is performed in stereotaxic space using BEaST followed by T1 tissue segmentation (Eskildsen et al., 2012, Avants et al., 2011). Subsequent PET processing steps include coregistration of the T1 image to the PET image using minctracc, masking, partial-volume correction, and quantification. The partial volume correction (PVC) method tested is the GTM method. The superiority of dynamic over static PET imaging was discussed in 2.2.1.1, and DVR images have demonstrated better performance in evaluating the accumulation of Aβ with the PiB radiotracer (Fujiwara et al., 2016). Thus, we also tested intensity normalization of the PET signal using the SUVR and Logan Plot DVR methods with the cerebellar cortex as the reference region.

3.4 Epidemic Spreading Model

The spread of Aβ was simulated using ESM, a diffusion model that has previously been used to simulate the spread of Aβ (or tau) in the ADNI dataset from an initial epicenter and through ROIs that the epicenter is connected to (Iturria-Medina et al., 2014; Vogel et al., 2019). In addition to the connectivity between ROIs, subject-specific propagation parameters dictate the spreading pattern. These parameters correspond to a global clearance rate, global production rate, and age of onset. These are fit by solving a non-linear differential equation designed to reproduce the overall regional pattern of Aβ deposition. ESM is fit by searching the parameter space, and the set of parameters that yield the regional pattern of Aβ deposition most similar to the reference (observed) pattern is selected.

3.4.1 Cross-sectional ESM

The main data input to the ESM is an ROI by Subject matrix reflecting the level of Aβ deposition in each region for each subject. The ESM is a probabilistic model, so each entry in this matrix is between [0, 1]. The ESM can also be run by pre-specifying

epicenter(s) or by allowing the model to select the most likely epicenter(s) in a data-driven way. When the latter is the case, based on how many epicenters the model is allowed to select, the ESM simulates the spread of Aβ using each combination of n epicenters and selects the combination that best explains the regional Aβ deposition at the group-level.

The overarching equation of the model is as follows:

$$\frac{dP_i}{dt} = (1 - P_i(t))\varepsilon_i(t) - \delta_i(t)P_i(t) + \aleph \tag{3.1a}$$

In (3.1a), the variables are:

$$\varepsilon = \sum_{j=1}^{N} \beta_j(t - \tau_{ij})C_{ij}(t - \tau_{ij})P_j(t - \tau_{ij})$$

C_{ij} = probability of fiber connections

β = MP production rate

δ = MP clearance rate or the probability of being clean of MP at time t

τ_{ij} = time delay which depends on MP propagation speed and length of fiber tracts

P_j = Probability of ROI j being infected some time delay before time t

$\aleph$ = e.g. effect of therapy being administered at time t

(3.1b)

Equation 3.1a posits that the change in probability of Aβ deposition in ROI ai is equal to the probability of receiving MP from ROIs connected to it or from itself minus the probability of clearing the deposited MP plus or minus some stochastic noise.

As was mentioned in Chapter 2, an ROI can be endogenously or exogenously infected according to the ESM. Hence, $\varepsilon_i(t)$ breaks down into:

$$\varepsilon_i(t) = \sum_{j \neq i} Pa_{j \to i}\beta_j^{ext}(t - \tau_{ij})P_j(t - \tau_{ij}) + Pa_{i \to i}\beta_i^{int}(t)P_i(t) \tag{3.2}$$

The two parts of the equation refer to the exogenous and endogenous causes of Aβ accumulation in an ROI i. The exogenous influence is the product of the weighted anatomical connection probability between ROI i and ROI j ($Pa_{j \to i}$), the extrinsic "infection" rate of ROI j with some time delay accounting for time it takes Aβ to propagate ($\beta_j^{ext}(t - \tau_{ij})$), and the probability of ROI j being infected at time t minus the delay ($P_j(t - \tau_{ij})$). The endogenous/intrinsic cause of MP accumulation captures intra-regional Aβ spread.

The extrinsic and intrinsic probabilities of soluble Aβ staying within an ROI or

diffusing out to other ROIs are governed by the basic principles of diffusion; Aβ propagates from regions of high concentration to regions with low Aβ concentrations. The equations for these probabilities are the following:

$$\begin{aligned} \beta_i^{ext}(t) &= g(t)\beta_i(t) \\ \beta_i^{int}(t) &= (1 - g(t))\beta_i(t) \\ \beta_i(t) &= \beta_i^{ext}(t) + \beta_i^{int}(t) \end{aligned} \tag{3.3}$$

$g(t)$ is modeled after the classic Gini coefficient, a measure of variability in data. The value ranges from [0, 1] where 0 corresponds to perfect equality and 1 corresponds to a total inequality. In other words, $g(t)$ dictates how likely it is that some amount of Aβ will either stay within an ROI or propagate to other ROIs. $\beta_i(t)$ denotes the regional MP deposition probability, and it is modelled as a sigmoidal function of the regional Aβ probability. This leaves us with:

$$\beta_i(t) = \beta_i(P_i, \beta_0) = 1 - e^{-\beta_0 P_i(t)} \tag{3.4}$$

Finally, $\delta_i(t)$ describes the probability of a region being clean of Aβ following "infection". Regional Aβ presence causes cell death by negatively impacting mitochondrial function - thus, regional capacity to clear deposited Aβ is reduced with an increased presence of Aβ (Readnower, Sauerbeck, and Sullivan, 2011). With that in mind, regional MP clearance was modeled with a decreasing sigmoidal function:

$$\delta_i(t) = \delta_i(P_i, \delta_0) = e^{-\delta_0 P_i(t)} \tag{3.5}$$

Note that both β_0 and δ_0 are unknown constant parameters that vary from [0, $+\infty$] and are expected to be influenced by the disease factor being assessed. $\aleph$, the variable representing noise, is assumed to have a Gaussian distribution with mean μ and standard deviation σ.

3.4.2 Longitudinal ESM

To test the ESM longitudinally, we made several modifications to the ESM workflow. We now use the Aβ pattern at the first timepoint as the initialization and Aβ pattern at the second timepoint as the reference pattern to simulate. For each subject, the parameter combination that results in a pattern most similar to the reference pattern is selected (Figure 3.1).

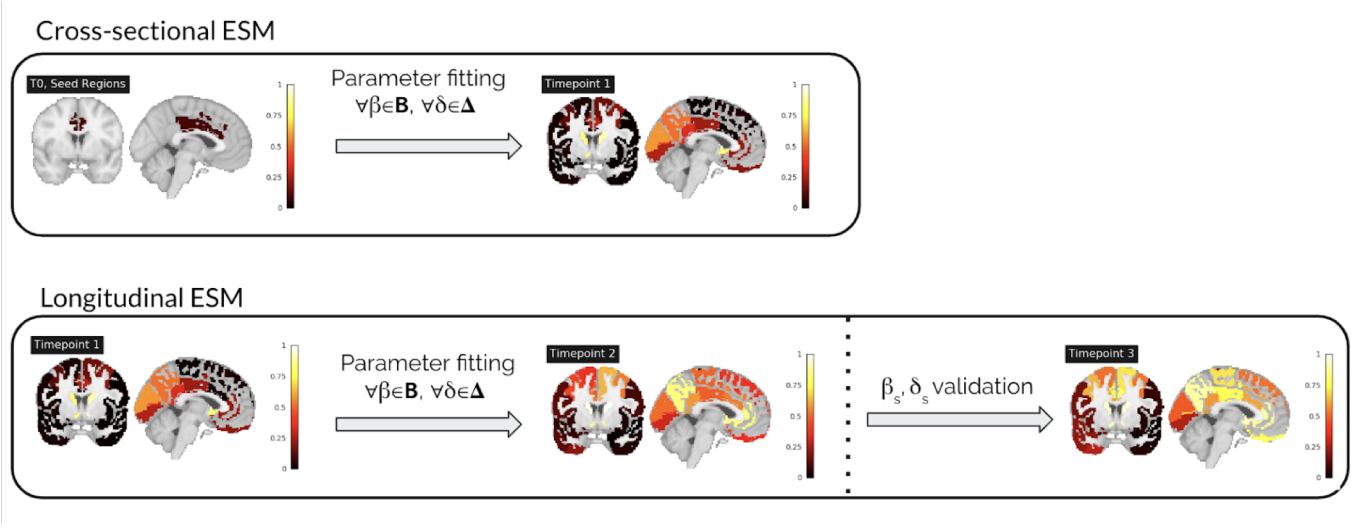

Figure 3.1: (a) Cross-sectional workflow. (b) Longitudinal workflow.

3.4.3 Pre-processing choices

As was shown in Vogel et al., 2019, ESM performance may be affected by the steps taken to preprocess PET data, the method used to quantify Aβ probabilities, the connectivity measure used, and the composition of the subjects. In 3.5, we describe the different probability metrics we applied to either co-registered PET images or parametric SUVR or DVR issues.

In 3.6, we describe the two measures of connectivity used in this thesis.

3.5 Regional Aβ Quantification

To quantify PiB PET signal regionally, we created subject-specific segmentations differently based on the PET processing pipeline used. For use with PUP, Freesurfer was used to derive subject-specific segmentations corresponding to regions in the Desikan-Killiany-Tourville atlas (DKT, Desikan et al., 2006). Only cortical and subcortical regions overlapping with the Mindboggle DKT atlas were used, for a total of 78 regions (Klein and Tourville, 2012). For APPIAN, users can define ROIs using a stereotaxic atlas, so we used the Mindboggle atlas and each subject's transform from their native T1 space to stereotaxic space to create subject-specific parcellations.

Traditionally, static PET processing involves quantifying co-registered PET images using standardized uptake value ratios (SUVR) for each ROI with respect to the average signal in a reference region devoid of specific tracer binding. The reference region typically used in AD Aβ PET imaging studies is the cerebellar cortex; however, amyloid deposition has been observed in the cerebellar cortex of individuals with

fAD (Bateman et al., 2010). Based on recent work seeking to clarify what an optimal reference region is for Aβ measurement using PiB-PET and the DIAN cohort, we tested both cerebellar cortex and brainstem as reference regions (Su et al., 2016, **landauOptimizingLongitudinalAmyloidv2018**). For the longitudinal ESM we used the brainstem as the reference region and provide justification for this in **??**. In addition to differences encountered using the two reference regions, the final regional Aβ probabilities may differ based on the data normalization method used to quantify them. Depending on how the PET data was processed, we can either use a voxelwise or regional normalization method. For instance, we did not have parametric SUVR or DVR images provided by PUP, so we could use a voxelwise probability metric with the co-registered PET scans or a regional probability metric with the mean regional SUVR or DVR values provided by the DIAN team.

The original ESM paper introduced a voxelwise probability metric, which we will refer to as V ECDF, RR EVD. This approach creates a bootstrapped sampling consisting of 40,000 subsamples in the 5-95% of values in the reference region. Subsequently, an extreme value distribution (EVD) is created using the maximum value observed in each bootstrapped sampling. The EVD is used to create an extreme cumulative distribution function (Fig 3.2b), and for each voxel in the PET image, the probability of it being greater than every value in the EVD is computed (Fig 3.2c). A final regional Aβ deposition value is calculated as the average of the probabilities corresponding to each voxel in the ROI. Given the overall higher PiB-PET signal in the brainstem than the cerebellar cortex, we use the 75th percentile value rather than the maximum in each bootstrap sampling to create the EVD when using the brainstem as the reference region.

When processing the data using PUP, we observed that the PiB signal in noncarrers was negligible in all regions except for the globus pallidus, thalamus, and putamen. Subsequently, for each ROI across all available timepoints, the noncarriers' signal was used to create a ROI-specific null distribution, and for each mutation carrier, we calculated a z-score for their Aβ binding probability in the ROI with respect to the ROI-specific null distribution. Within each ROI, we min max scaled the absolute values of the z-scored signal across all timepoints to have probabilities in the [0,1] range again.

As described in 3.3, we used the GTM PVC method in a subset of the processing workflows. A caveat of using a regional PVC method is that we subsequently cannot use a voxelwise data normalization strategy, so we used a Gaussian mixture modelling approach which has been shown to be effective in detecting different distributions of Aβ (Villeneuve et al., 2015, Grothe et al., 2017). A regional GMM was first applied in Vogel et al., 2019, and this approach assumes that pathological

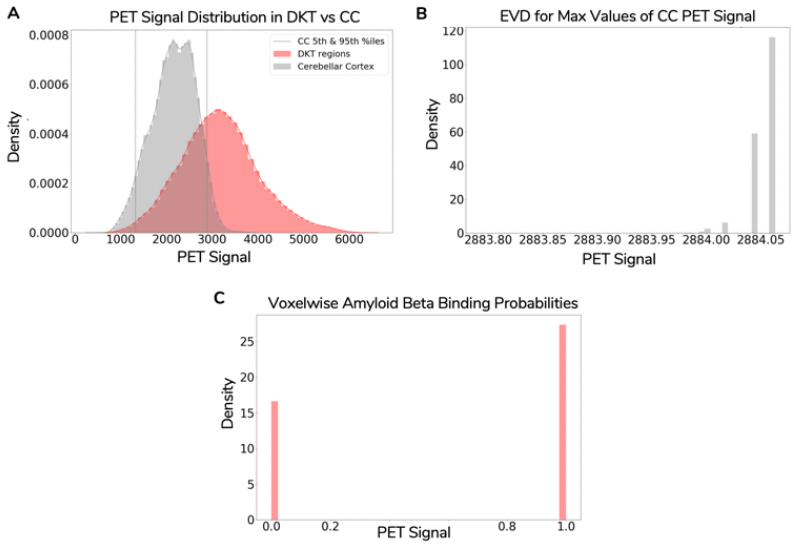

Figure 3.2: (A) An example mutation carrier's plot showing their PET signal distribution for the cerebellar cortex (CC) and DKT regions. (B) Bootstrapped distribution of max values in CC. (C) Distribution of DKT regional probabilities after creating an ECDF of the red signal in A with respect to the one in B.

signal can be described using a bimodal distribution where pathological signal is skewed while non-specific signal follows a normal distribution. For each region, one-component model and two-component models are fit, and the fit of each model is evaluated using Aikake's information criterion (AIC). If a one-component model is selected, that suggests that there is no pathological signal for the given region across the population. However, if a two-component model is selected, that suggests that there is indeed a pathological level of Aβ in a subset of the population. For regions whose distribution is best described using a two-component model, a region-specific SUVR or DVR threshold can be selected above which signal can be considered pathologic. As with the voxelwise reference strategy, we need to compute probabilistic values for use with the ESM. Thus, we compute the probability of each subject's ROI SUVR/DVR value falling onto the rightmost Gaussian distribution of that ROI. An example of the regional GMM method being applied to the left precuneus is depicted in Fig 3.3.

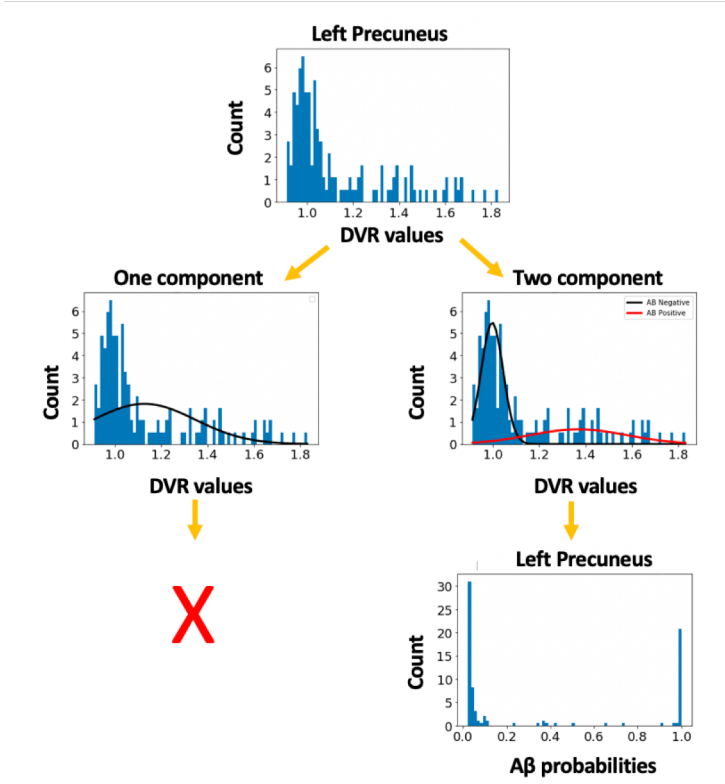

Figure 3.3: For each region - e.g. the left precuneus - a one component and two component model is fit. In this case, the best fitting one is the two-component one, and the one-component is rejected. Probabilities for every subject's value in the left precuneus is computed with respect to the rightmost distribution in the two-component model.

3.6 Connectivity Measures

In order to propagate Aβ signal across the brain, the ESM requires a matrix of pairwise relationships between ROIs. This informs the final regional pattern of Aβ. The original ESM paper tested whether Aβ spreads along synapses by using a structural connectivity matrix. Using a functional connectivity matrix, we can also test whether Aβ spreads indirectly. We can also use a relationship matrix corresponding to Euclidean distance to test whether Aβ spreads throughout the extra-cellular space, simply via spacial proximity.

3.6.1 Structural Connectivity

We used a structural connectivity matrix derived from diffusion spectrum imaging (DSI) scans of 60 young healthy subjects from the CMU-60 DSI template (Yeh and Tseng, 2011). The acquisition and preprocessing have been described in detail in the original ESM paper and were based on methodology developed in an earlier paper (Iturria-Medina et al., 2007, Iturria-Medina et al., 2014). Briefly, all images were nonlinearly co-registered to MNI space and orientation distribution functions

(ODF) representing nerve fiber orientations were calculated. All intravoxel fiber ODF maps were averaged to create an ODF template, and an automated fiber tractography method was used to calculate probabilistic axonal connectivity values for each voxel and the surface of each grey matter region in the DKT atlas. Previously described anatomical connection probabilities were then generated for each ROI-ROI pair.

3.6.2 Functional Connectivity

To create a functional connectivity matrix, we used all resting-state fMRI (rs-fMRI) scans available for non-carriers in the DIAN dataset. We pre-processed the scans using the default settings of fMRIPrep (Esteban et al., 2019).

After performing quality control for motion and registration, we were left with 200 scans. For each time-series, we used Nilearn (https://nilearn.github.io/) to regress out the following set of confounds computed by fMRIPrep - the average signal within anatomically-derived eroded CSF and white matter masks, six rigid-body motion parameters, framewise displacement, along with anatomical and temporal noise. Using the signal that has undergone confound regression, we computed a correlation matrix for each pair of 78 ROIs. We averaged across all correlation matrices to create an average resting state connectivity matrix specific to the DIAN dataset. All values were min max scaled to be between 0 and 1.

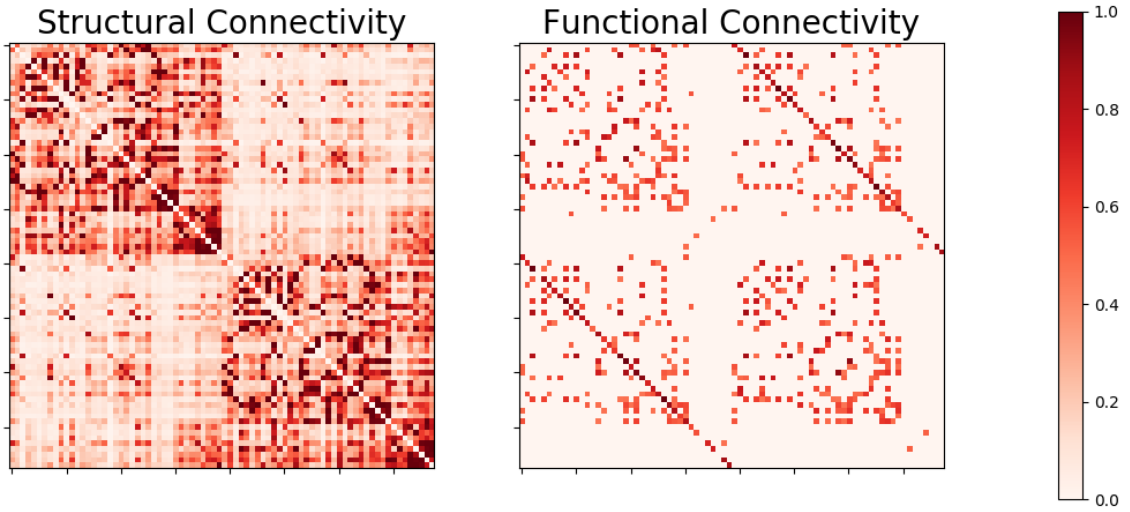

Figure 3.4: (a) Structural connectivity matrix from CMU-60 DSI dataset. (b) Functional connectivity matrix from DIAN participants. The functional connectivity matrix has fewer highly weighted connections. Unlike the FC matrix, the SC matrix does not exhibit homotopic connections.

3.7 CSF measures

In addition to PET based detection of Aβ load in the brain, CSF measures of Aβ1-42, tau, and phosphorylated tau have served as useful early biomarkers of AD and can often be detected earlier than a buildup of Aβ plaques in the brain. Mounting evidence has pointed to Aβ further spurring tauopathy, and the original application of the ESM to the ADNI dataset demonstrated that model parameters related to Aβ progression can in fact explain a substantial amount of variance in CSF tau as well as Aβ.

In addition the neuroimaging measures of Aβ, we used CSF measures Aβ1-42, tau, and phosphorylated tau in subsequent statistical analysis. All CSF samples were analyzed by the DIAN Biomarker Core at Washington Universtiy. CSF concentrations of Aβ1-42, tau, and ptau181 were measured by immunoassay using Luminex bead-based multiplex technology (INNO-BIA AlzBio3, Innogenetics, Ghent, Belgium). Detailed processing steps have previously been described (Fagan et al., 2014).

3.8 Statistical Analysis

3.8.1 Cross-sectional Analysis

Using the different connectivity and PET preprocessing methods we evaluate how well the ESM reproduces baseline Aβ deposition patterns across different input combinations. We evaluate model performance both within-subject and at the group-level. Within-subject accuracy is defined as the r^2-value between the observed and predicted regional Aβ probabilities for a given subject, and we report the average within-subject accuracy as well as a comparison of performance between the PSEN1, PSEN2, and APP mutation types. (3.6a).

$$\begin{aligned} r_n^2 &= \rho(ref_n, pred_n)^2 \\ r_{n,avg}^2 &= \sum_{n=0}^{N} (r_n^2)/N \end{aligned} \tag{3.6a}$$

In 3.6a, the variables are:

$$\begin{aligned} ref_n &= \text{reference regional A}\beta\text{ pattern for a subject} \\ pred_n &= \text{predicted regional A}\beta\text{ pattern for a subject} \end{aligned} \tag{3.6b}$$

Group-level performance is calculated as how well the ESM reproduces the baseline aggregated Aβ deposition patterns, where we compute the r^2 between the average observed and predicted regional Aβ levels (3.7a). To assess statistical significance of our results given the connectivity matrix used, we create 100 randomized versions of the original structural connectivity matrix where the distribution of strength, degree, and weight is preserved. Using each of these randomized matrices, we fit the ESM again. A p-value for our original model is computed based on whether its aggreggated performance is higher than that of the models using the randomized matrices. Because we use 100 randomized matrices, the lowest p-value can be 0.01. Additionally, we evaluate how well the ESM does at an individual level based on how much cortical Aβ a subject has.

$$\begin{aligned} ref_{ROI_i,group} &= \sum_{n=0}^{N} (ref_{ROI_i,n})/N \\ pred_{ROI_i,group} &= \sum_{n=0}^{N} (pred_{ROI_i,n})/N \\ r^2_{group} &= \rho(ref_{group}, pred_{group})^2 \end{aligned} \tag{3.7a}$$

In 3.7a, the variables are:

$$\begin{aligned} ref_{ROI_i,n} &= \text{reference A}\beta \text{ probability for a given subject } n \text{ at ROI } i \\ pred_{ROI_i,n} &= \text{predicted A}\beta \text{ probability for a given subject } n \text{ at ROI } i \end{aligned} \tag{3.7b}$$

Because most mutation carriers at baseline are cognitively normal, we define mutation carriers who have a global CDR > 0 as symptomatic and those with a global CDR = 0 as asymptomatic. Using a t-test, we compare whether there are group differences in the subject-level ESM parameters between those who are asymptomatic vs symptomatic.

We ascertain whether there is a significant relationship between regional Aβ probabilities and the average effective anatomical distance between ROIs and the epicenters for both asymptomatic and symptomatic subjects. Effective anatomical distances were estimated as the length of the shortest path linking each region i with the epicenters from the best-fitting model.

In Iturria-Medina et al., 2017, the authors propose that if the ESM can accurately recapitulate intra-brain spatial patterns of Aβ, then it follows that the subject-specific parameters governing Aβ production and clearance may reflect individual levels of Aβ in the CSF. Furthermore, given the interplay between Aβ and tau, the ESM parameters may explain CSF levels of tau and phosphorylated tau. Subsequently, we

performed a six-way ANOVA test, considering the Aβ production rate, Aβ clearance rate, Aβ onset age, age, gender and educational level as modulatory factors of the three aforementioned CSF measures.

3.8.2 Longitudinal analysis

Using the combination of preprocessing choices that allowed us to best reproduce Aβ deposition patterns cross-sectionally (Aim 1), we sought to now use the ESM longitudinally to evaluate parameter differences between individuals who are accumulating Aβ and assess whether parameters fit between two timepoints can be used to predict the regional rate of change in Aβ between timepoints (Aim 2).

As described in 3.4.2, we use data from multiple timepoints to run the ESM longitudinally. Here we evaluate how well the ESM can reproduce not the overall reference pattern but the regional rate of change in Aβ probabilities between the first and second timepoint. We compute the r^2 between the average observed and average predicted regional rate of change for prefrontal, orbitofrontal, parietal, temporal, anterior cingulate, and posterior cingulate/precuneus ROIs for each subject. To test how significant our results are, we once again fit the ESM over 100 randomized versions of the original structural connectivity matrix.

Ultimately, we are interested in whether ESM can reproduce regional Aβ accumulation, and for simpler visualization, we opted to split all MC into those who are accumulating Aβ between timepoints and those who are not accumulating. We defined mutation carriers whose mean rate of change in Aβ probabilities was greater than twice the standard deviation (SD) of the noncarriers' average rate of change for the cortical regions between for the first two timepoints as accumulators. We assessed ESM parameter differences between accumulating versus non-accumulating mutation carriers using an independent two-tailed t-test.

ESM uses a grid-search method to select the best subject-specific global clearance and production parameters, and we were interested in evaluating how much better ESM performs using the selected parameters compared with the whole range of possible clearance and production parameter combinations. The ESM cost function is the reciprocal of the Euclidean distance (ED) between the observed and predicted pattern, so for each subject, we normalized the reciprocal of the ED for every production and clearance combination to be between [0,1]. To account for how well ESM explained the short-term change in Aβ probabilities for each subject, we normalized all of the subjects' performance to be between [0,1] and multiplied each subject's normalized ED value at every parameter value combination by their normalized within subject r2-value.

To assess whether parameters fit between the first two timepoints can be used to predict the rate of change in Aβ between the second timepoint and a future timepoint, we compute the r^2 between the observed and predicted within subject regional rate of change in Aβ probabilities between timepoints 2 and 3.

Chapter 4

Results

4.1 Conversion to Aβ deposition probabilities

For the mutation carriers whose baseline scans were available, we created subject by ROI Aβ deposition probability matrices using the different strategies presented in section 3.5. Figure 4.1 illustrates the matrix produced from applying the V ECDF, RR EVD method introduced in Iturria-Medina et al., 2014. In this case, using the brainstem as the reference region, the raw co-registered PET signal was converted to regional probabilities of Aβ deposition. With the subjects with the least to most Aβ across all regions sorted from top to bottom and regions with the least to most Aβ across all subjects sorted from right to left, we can visualize a pseudotemporal progression of Aβ deposition. In keeping with recently proposed ordering of Aβ accumulation in LOAD patients (Mattsson et al., 2019), we see that regions such as the posterior cingulate, medial orbitonfrontal cortex and precuneus have high levels of Aβ, suggesting that they accumulate Aβ earlier in the disease timecourse. However, we note that the subcortical regions such as the thalamus, globus pallidus, caudate, and putamen also have high binding.

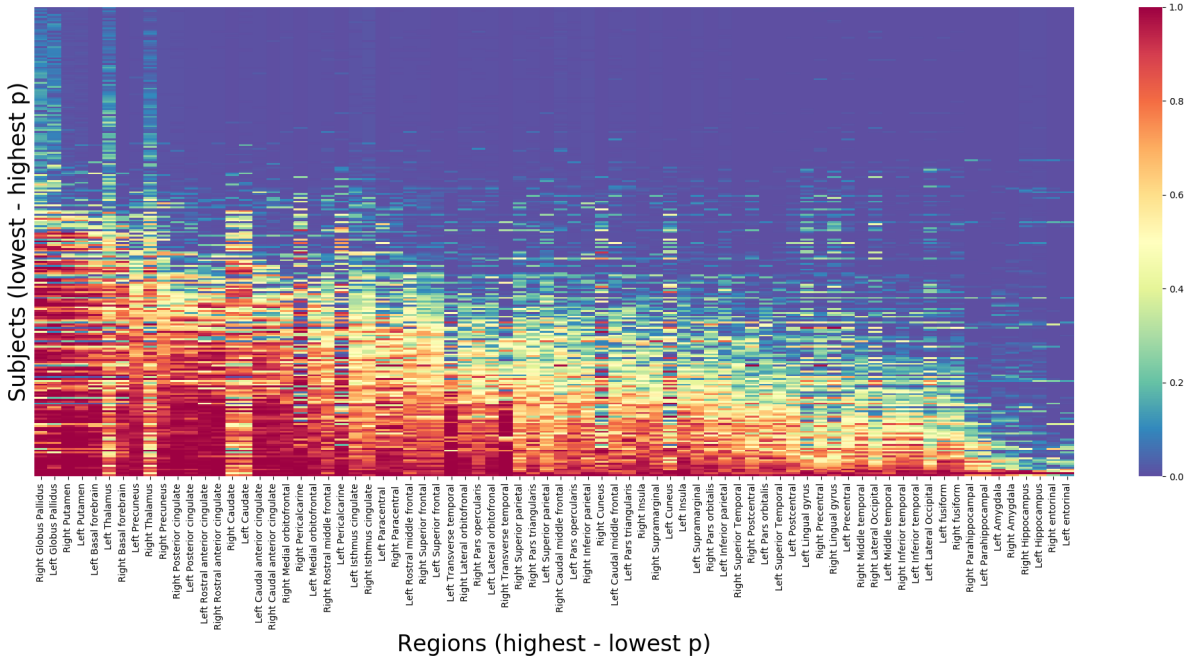

Figure 4.1: Aβ data following conversion using voxelwise EVD reference strategy. Matrix is sorted with subjects with the highest Aβ probabilities (p) across all regions towards the bottom and regions with the highest Aβ probabilities across all subjects towards the left. Neocortical areas such as the posterior and caudal anterior cingulate, precuneus, rostral anterior cingulate and caudate exhibit the highest levels of Aβ across all subjects.

4.2 Reproducing baseline Aβ deposition patterns in DIAN

4.2.1 Cross-sectional model performance

The ESM was fit to the baseline data of mutation carriers, simulating the spread of Aβ from a set of seed regions. The ESM was fit using PiB data using different pipelines and methods to compute regional Aβ positivity. In addition to (i) PET processing, we tested the impact of (ii) seed regions and (iii) choice of connectivity measure. Different numbers of subjects were available depending on the type of processing done. The results for all tested combinations of model parameters is reported in Table 4.1.

4.2.1.1 Structural Connectivity

Overall, models performed better when fit over a structural connectivity matrix. Performance was further improved using PiB scans preprocessed using PUP. When using APPIAN to pre-process PET scans, better ESM performance was achieved using the V ECDF, RR method introduced in 3.5.

The seed regions explaining the most variance in the baseline group-level spatial pattern of Aβ were the medial orbitofrontal cortex, precuneus, and posterior cingulate, irrespective of the reference region used for PET processing. The best-fitting model using the cerebellar cortex as the reference region (model A) explained 44% (null model mean r2 [95% CI] = 0.11 [0.077, 0.157]; $p < 0.01$) of the aggregated pattern of Aβ and on average explained 22% (null model mean r2 [95% CI] = 0.092 [0.077, 0.11]; $p < 0.01$) of the regional pattern of Aβ in individual subjects.

The best-fitting model using the brainstem as the reference region (model B) explained 35% (null model mean r2 [95% CI] = 0.088 [0.057, 0.128]; $p < 0.01$) of the aggregated pattern of Aβ and on average explained 17% (null model mean r2 [95% CI] = 0.065 [0.054, 0.082]; $p < 0.01$) of the regional pattern of Aβ in individual subjects.

4.2.1.2 Functional Connectivity

Recently it has been shown that the spread of tau can be reproduced using both functional and structural connectivity, so we sought to assess whether just changing the source of connectivity information would result in comparable ESM performance (Vogel et al., 2019). Using the set of cortical epicenters that explained the most variance, we were not able to achieve similar subject-level or group-level performance using functional connectivity (4.1). Depending on whether the Aβ deposition probabilities were computing using the cerebellar cortex or brainstem as the epicenter, the accuracy was 1% and 12% for reproducing the aggregate baseline Aβ pattern, respectively.

4.2.1.3 Group-level ESM performance

In addition to evaluating group-level performance across the disease timecourse, we binned subjects into groups based on their estimated years to symptom onset. In 4.2, we show a qualitative and quantitative assessment of ESM performance staggered across the set of EYO ranges (-20 to -10, -10 to 0, 0 to 10, and 10 to 20 EYO) for models A and B. In 4.2A,C, we see that for both models, the ROIs that appear to accumulate Aβ most quickly are in fact the posterior cingulate, precuneus, and medial orbitofrontal cortex, those ROIs that have been identified as areas of early accumulation (Mattsson et al., 2019). There is an initial discord between the observed and predicted pattern for the cuneus and lingual gyrus, regions that have been pinpointed as areas of intermediate and late accumulation, but they do in fact appear to have higher Aβ probabilities later in the disease timecourse compared with the aforementioned early accumulating regions.

One discernable difference between Model A and Model B is that the Aβ deposition probabilities are lower in Model B as a result of the reference region being used,

and this appears to negatively impact the group-level performance in EYO ranges that are further from estimated symptom onset.

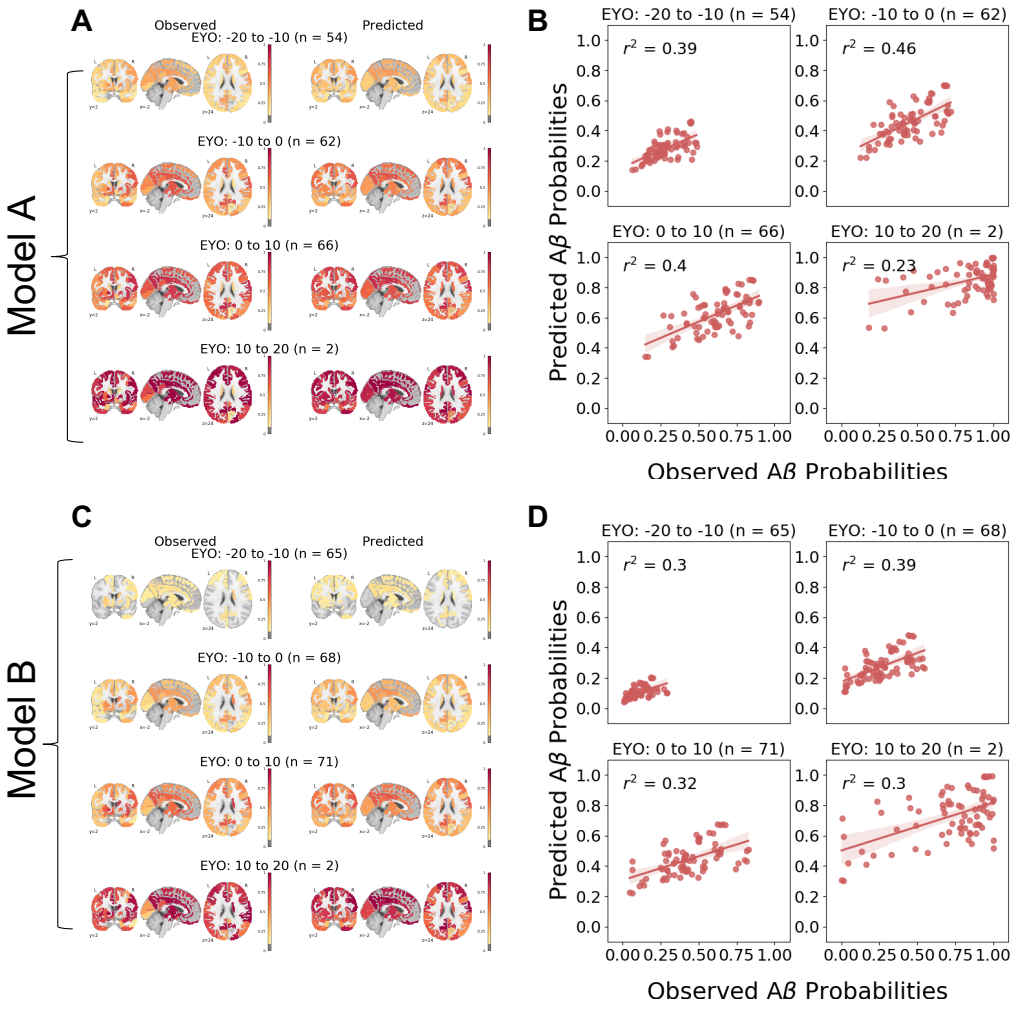

Figure 4.2: (a) Model A: A qualitative evaluation of model performance depicting the average observed regional probabilities (left) and the values predicted by the ESM (right) for model and (b) the quantitative evaluation within the same EYO ranges. (c) Model B: A qualitative evaluation of model performance depicting the average observed regional probabilities (left) and the values predicted by the ESM (right) for model and (d) the quantitative evaluation within the same EYO ranges.

4.2.1.4 Within-subject performance across mutation types and epicenters

Given the fact that Model B appears to be more sensitive than Model A to the non-negligible presence of Aβ, we opted to split subjects into those who are Aβ positive vs Aβ negative for an average Aβ deposition probability across a set of cortical ROIs that have previously been used by the DIAN Imaging Core to determine Aβ positivity using SUVR values. These cortical regions are comprised of the precuneus, superior frontal, rostral middle frontal, lateral orbitofrontal, medial orbitofrontal, superior

temporal, and middle temporal cortex. In the ESM, only the initial epicenters are assumed to have Aβ, and they are assigned an Aβ deposition probability of 0.1. Thus, for this analysis, we categorize individuals as Aβ positive if they have an average probability of 0.1 across these cortical ROIs.

In Figure 4.3, we compare within-subject performance using either the caudate and putamen or the set of best-performing cortical regions as epicenters. The only mutation type for whom performance is high using the caudate and putamen as the epicenter is PSEN1, and this holds only for individuals who are Aβ negative with respect to cortical regions. Overall, the within-subject performance is significantly higher in 4.3A.

We only show the results from experiments that used Aβ deposition probabilities, but the results were comparable with those using the cerebellar cortex as the reference region.

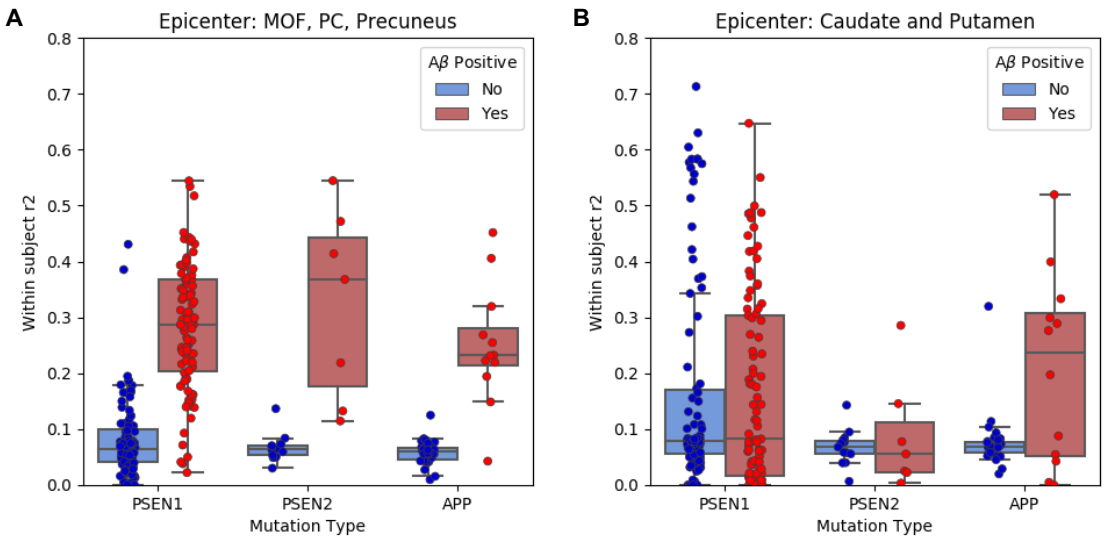

Figure 4.3: (a) Within subject performance as a function of mean cortical Aβ probabilities. Using the brainstem as the reference region results in more subjects being considered Aβ negative, and ESM fit is negatively impacted by that. However, Model B's performance is consistently higher for Aβ positive individuals. (b) Model B performance for four exemplary subjects, all of whom are cognitively normal. Each dot is an ROI and is colored according to its status in the Mattsson staging system.

Table 4.1: Baseline results using different models

Pipeline	N (MC)	Ref Region	Quant PET Method	PVC	Normalization	Conn Matrix	Seed Regions	Data-driven seeds	Mean Subject R2	Global R2
APPIAN	78	CC	SUVR	No	V ECDF, RR	ACP	L Pericalcarine, R Post Cing	Yes	0.131	0.19
APPIAN	82	CC	DVR	No	V ECDF, RR	ACP	L/R Precuneus, PC, MOF	No	0.135	0.175
APPIAN	108	CC	SUVR	No	V ECDF, RR	ACP	L/R Precuneus, PC, MOF	No	0.118	0.185
APPIAN	82	CC	DVR	No	GMM	ACP	L/R Precuneus, PC, MOF	No	0.085	0.17
APPIAN	82	CC	DVR	No	GMM	ACP	L/R Entorinal	Yes	0.083	0.031
APPIAN	108	CC	SUVR	No	V ECDF, RR	ACP	R Pericalcarine, L RAC	Yes	0.189	0.247
APPIAN	84	CC	DVR	Yes	GMM	ACP	L/R Precuneus, PC, MOF	No	0.104	0.214
APPIAN	84	CC	DVR	Yes	GMM	FC	L/R Precuneus, PC, MOF	No	0.072	0.128
APPIAN	84	CC	DVR	Yes	GMM	FC	L Entorinal, R Hypothalamus	Yes	0.161	0.019
APPIAN	84	CC	DVR	Yes	GMM	ACP	L Entorinal, R Hypothalamus	Yes	0.124	0.0003
PUP	134	CC	DVR	Yes	GMM	ACP	L/R Precuneus, PC, MOF	No	0.093	0.262
PUP	215	CC	None	No	V ECDF, RR EVD	ACP	L/R Precuneus, PC, MOF	No	0.22	0.44
PUP	215	CC	None	No	V ECDF, RR EVD	FC	L/R Precuneus, PC, MOF	No	0.15	0.12
PUP	249	BS	None	No	V ECDF, RR EVD	FC	L/R Precuneus, PC, MOF	No	0.08	0.01
PUP	215	CC	None	No	V ECDF, RR EVD	ACP	L PC, R CAC	No	0.16	0.27
PUP	249	BS	None	No	V ECDF, RR EVD	ACP	L/R PC, CAC	No	0.16	0.27
PUP	215	BS	None	No	V ECDF, RR EVD	ACP	L/R Putamen, Caudate	No	0.15	0.22
PUP	249	CC	None	No	V ECDF, RR EVD	ACP	L/R Putamen, Caudate	No	0.09	0.06
PUP	249	BS	None	No	V ECDF, RR EVD	ACP	L/R Precuneus, PC, MOF	No	0.17	0.35

The best performing models (model A and model B) are highlighted.
V ECDF, RR = Voxelwise ECDF with respect to reference region signal; **GMM** = Gaussian Mixture Model
ECDF NN = ECDF with respect to noncarriers' regional probabilities
V ECDF, RR EVD = Voxelwise ECDF with respect to extreme value distribution of reference region signal
ACP = Anatomical Connectivity Probability; **FC** = Functional Connectivity; **ED** = Euclidean Distance
PC = Posterior Cingulate; **MOF** = Medial Orbitofrontal Cortex; **RAC** = Rosterior Anterior Cingulate; **CAC** = Caudal Anterior Cingulate

4.2.2 Predicting regional Aβ arrival time with effective anatomical distance to outbreak region and connectivity degree

Previous application of the ESM to the Aβ probabilities of ADNI participants showed a significant negative association between effective anatomical distance to epicenter seed regions and regional Aβ probabilities, and we observed the same association with fAD mutation carriers, both for symptomatic and asymptomatic individuals (Fig 4.4). As was seen with the different clinical diagnoses in ADNI, the best fit lines for asymptomatic and symptomatic individuals are collinear. This result supports the idea that there are regions that serve as epicenters of Aβ accumulation, propagating Aβ to those regions that are connected to them.

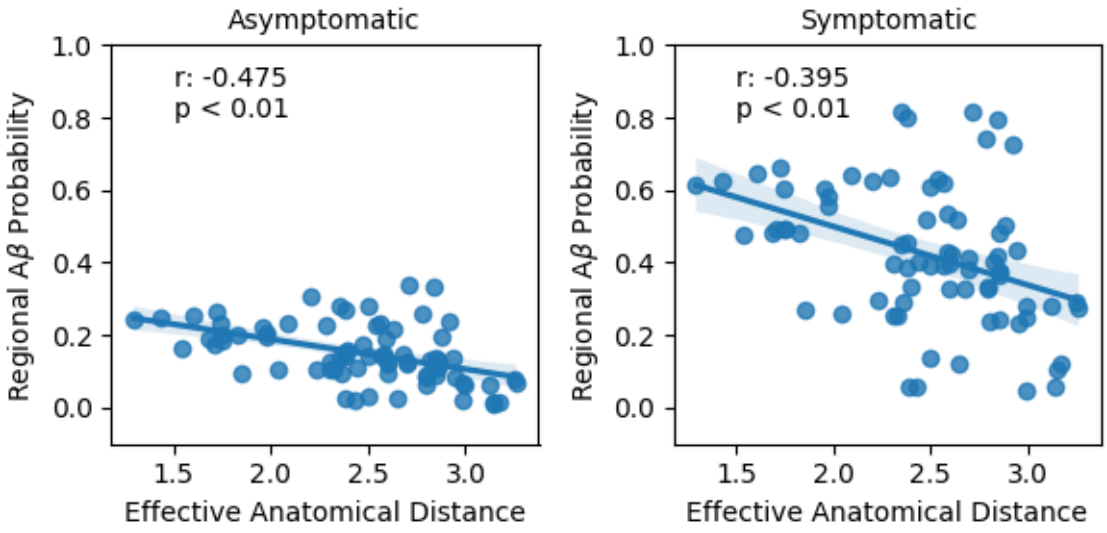

Figure 4.4: Regional Aβ probabilities for asymptomatic and symptomatic subjects vs effective anatomical distance.

4.2.3 Cross-sectional parameter analysis

We further extend our exploratory analysis of the effect of different PET processing methods by reporting the results from the statistical analyses described in 3.8 using subject-specific ESM parameters from both models A and B.

4.2.3.1 Clinical diagnosis is not driven by ESM subject-specific parameters

In Figure 4.5, we compare the production and clearance parameters across Aβ positive mutation carriers who are asymptomatic and symptomatic. While clinical changes in sporadic AD were related to reduced clearance (Iturria-Medina et al., 2014), we don't observe the same effect for ADAD mutation carriers. We are limited here by

a smaller sample size and a predominantly cognitively normal dataset, and cannot draw any conclusions about whether over-production or under-clearance of Aβ is linked to the emergence of cognitive symptoms. Since individuals who develop fAD are significantly younger than those who develop sAD, modulatory factors such as cognitive reserve have a more significant effect on when an individual will begin to exhibit cognitive symptoms. A six way ANOVA exploring the effects of the Aβ production rate, Aβ clearance rate, Aβ onset age, age, gender and educational level on Mini Mental State Examination (MMSE) scores showed that the only significant modulator was age, explaining 8.78% (P=3.55e-02, F=4.655) of the variance in MMSE scores. These results were consistent across Model A and Model B.

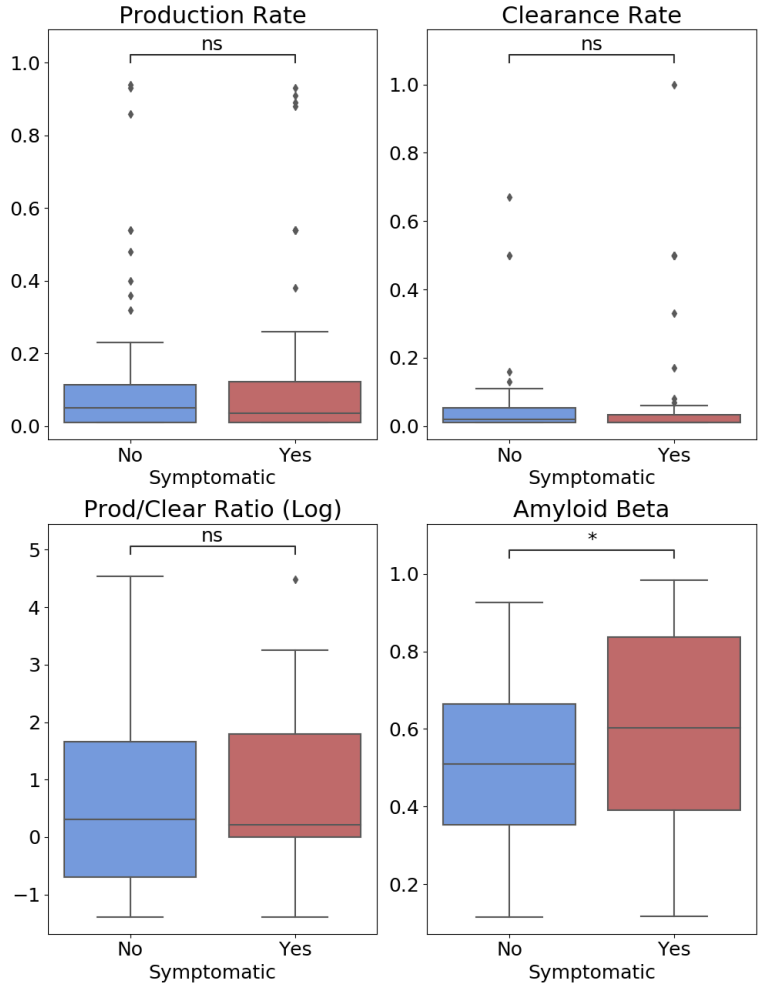

Figure 4.5: From left to right - clearance, production, production/clearance ratio, and mean cortical Aβ probability for asymptomatic vs symptomatic mutation carriers who are Aβ positive. Neither the subject-specific clearance nor production parameters are significantly different between the cohorts. *p < 0.05.

4.2.3.2 CSF measures

We performed a six-way ANOVA test, considering the Aβ production, Aβ clearance rate, Aβ onset age, age, gender, and educational level as modulatory factors of CSF Aβ1-42, tau, and phosphorylated tau.

The ANOVA results vary across Model A and Model B. For Model A, Aβ production rates explained 5.82% (P=1e-03, F=11.5) of the variance in CSF Aβ1-42 levels. For the CSF tau levels, age, and education explained 2.77% (P=2.2e-02, F=5.36) and 3.99% (P=6e-03, F=7.72), respectively. For CSF p-tau, the Aβ production rate and Aβ clearance rate explained 2.23% (P=4e-02, F=4.29) and 2.52% (P=2.9e-02, F=4.85). The relationships between the CSF measures and ESM parameters derived using Model B were weaker and are depicted in Table 4.2.

Across the different models whose results we analyzed, there are notable discrepancies between the modulatory effects of the Aβ progression parameters, and it is difficult to definitively conclude which relationships are the most meaningful given the lack of consistency.

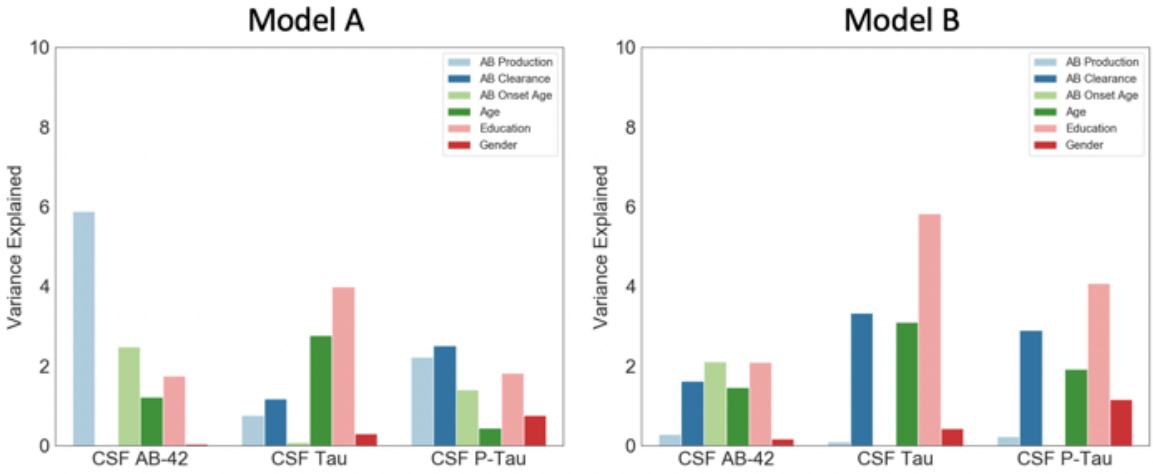

Figure 4.6: We assessed the relationship between model parameters, demographic variables and CSF levels of Aβ, tau, and p-tau across the best-fitting models. While Aβ production appears to be strongly related to CSF Aβ1-42 and p-tau levels in Model A, this effect is not reproduced in Model B.

Table 4.2: % Variance Explained in CSF Aβ1-42, tau, and p-tau by model parameters (all subjects)

	Gender	AB Prod.	AB Clear.	AB Onset	Age	Education
CSF AB42 (A)	0.04 (ns)	5.89 (***)	0.02 (ns)	2.48 (*)	1.22 (ns)	1.75 (ns)
CSF Tau (A)	0.3 (ns)	0.77 (ns)	1.18 (ns)	0.09 (ns)	2.77 (*)	3.99 (**)
CSF PTau (A)	0.76 (ns)	2.23 (*)	2.52 (*)	1.41 (ns)	0.45 (ns)	1.82 (ns)
CSF AB42 (B)	0.18 (ns)	0.29 (ns)	1.63 (ns)	2.11 (*)	1.47 (ns)	2.1 (*)
CSF Tau (B)	0.43 (ns)	0.1 (ns)	3.33 (**)	0.00 (ns)	3.11 (**)	5.83 (**)
CSF PTau (B)	1.17 (ns)	0.23 (ns)	2.90 (*)	0.03 (ns)	1.92 (*)	4.08 (**)

Each entry corresponds to the % variance explained by the modulatory variable on the CSF variable of interest (p-value).
*p $\leq$ 0.05, **p $\leq$ 0.01, ***p $\leq$ 0.001, **** $\leq$ 0.0001. **A** = Model A;
B = Model B;
AB Prod = Aβ production rate; **AB Clear** = Aβ clearance rate; **AB Onset** = Aβ onset age.

4.3 Longitudinal model training and validation

4.3.1 Selecting a reference region

The results of Table 4.1 indicate that Model A and B perform best, and we decided to use the combination of processing steps used in Model B for all longitudinal analysis because the brainstem has previously been shown to be a better reference region for distinguishing between mutation carriers and noncarriers longitudinally (Su et al., 2016), and we show that that holds in Figure A1. In Figure 4.7, we depict the average rate of change in Aβ in mutation carriers within a set of cortical ROIs with respect to their years to symptom onset and the baseline Aβ deposition in those ROIs.

4.3.2 Training

As described in section 3.4, we fit a subject's regional Aβ pattern at the second scan to that at the first, and let the ESM select the parameters that best explain the change in regional values over time. We will refer to the longitudinal ESM as Model C.

Model C explained on average 75.2% of the regional pattern of Aβ within subjects at timepoint 2. However, what we assess now is how well the model can explain the regional rate of change in individual subjects since a subject's scans are highly correlated between visits. Model performance was very variable; the mean individual r2 was 30.9% with an SD of 24.1% (mean RMSE = 0.048, SD = 0.031). Unlike what we observed with the cross-sectional analysis, longitudinal ESM fit was not significantly better using the original structural connectivity matrix rather than the randomized versions of this matrix (null model mean individual r2 = 27.1% and SD = 34.5%; p = 0.98).

As we can see in Figure 4.7, many subjects do not show much change between visits, so we explored whether there were specific trends amongst individuals or regions for whom the ESM performed well. We found that for individuals who

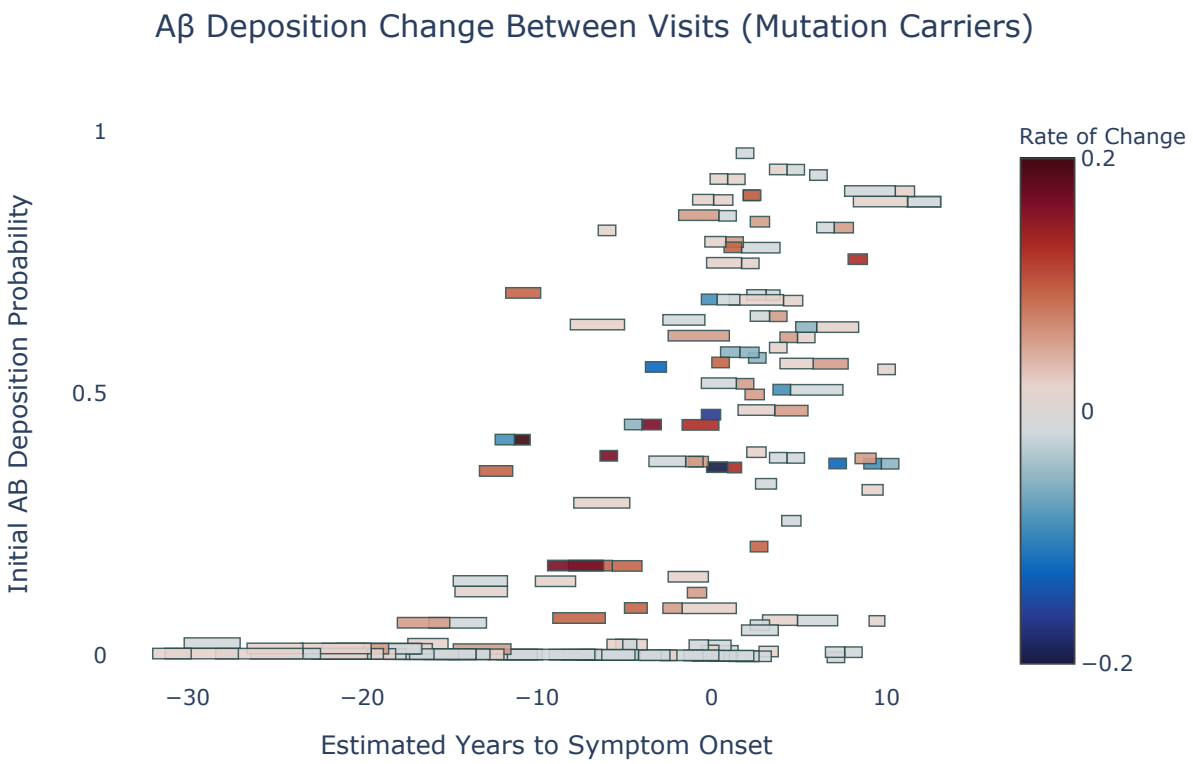

Figure 4.7: Both within and across individuals, there is substantial heterogeneity in rates of Aβ accumulation across the disease timecourse.

consistently had positive or no change in regional Aβ levels, the ESM performed well (Fig 4.8). The ESM did not perform as well for subjects who had inconsistent amounts of negative and positive change, and we attribute this to the ESM being unable to simulate some regions undergoing atrophy while others accumulate Aβ.

The ESM was able to explain changes in regional Aβ values best for those regions that tend to have higher PiB-PET signal, e.g. the precuneus, caudal anterior cingulate, posterior cingulate (Fig 4.9). Conversely, for regions that have lower PiB-PET signal across all mutation carriers, the ESM was not able to explain the rate of change between visits as well.

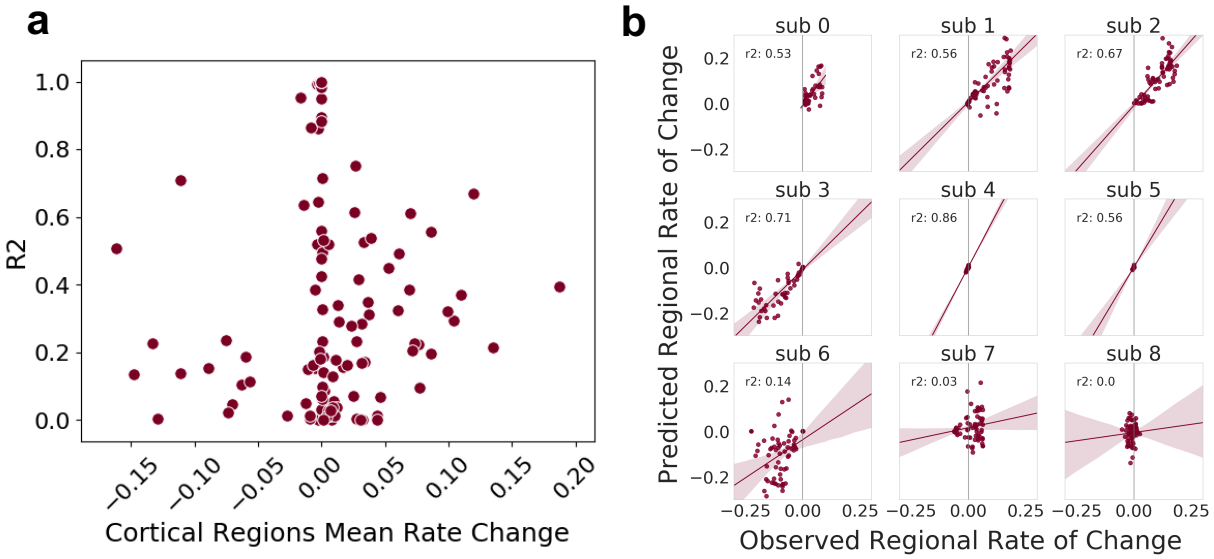

Figure 4.8: (a) Each dot is a subject, and we show the association between each subject's average rate of change in cortical regions and Model C's performance in reproducing these rates of change within subject. (b)Performance for individual subjects, each dot is an ROI. A line is drawn at 0 to help distinguish subjects who have an overall positive rate of change in all regions. Model C performs very well for those subjects who are consistently accumulating Aβ (subs 0, 1, 2) or showing no change between visits (subs 4, 5). Within subject performance for those subjects who show decreases in Aβ is not consistently high (subs 3,6), and the model cannot reproduce regional rates of change that are both negative and positive (subs 7, 8).

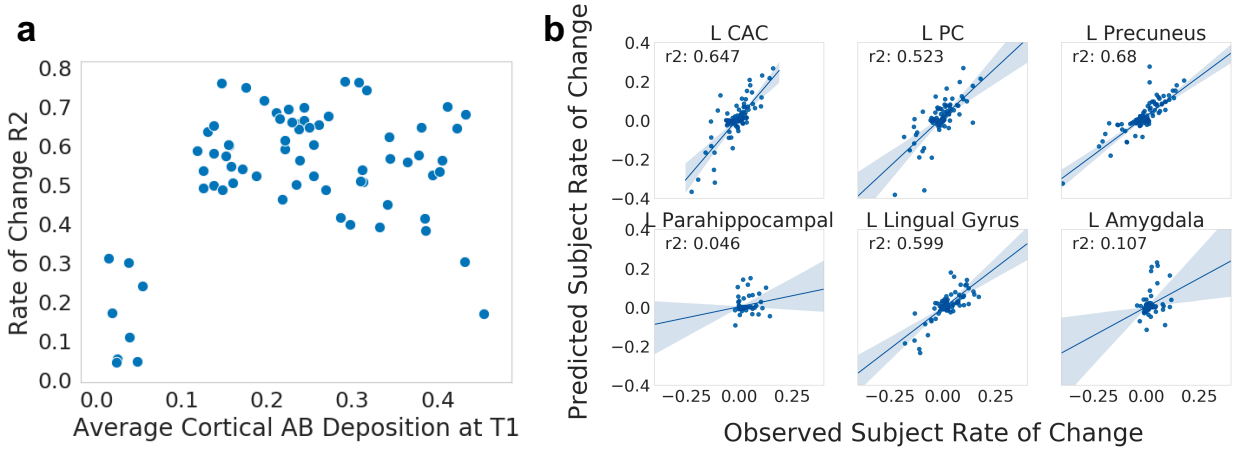

Figure 4.9: (a) Each dot is an ROI, and we show the association between average Aβ deposition in an ROI and longitudinal model performance for the ROI. (b) Performance on exemplar regions, each dot is a subject.

4.4 Longitudinal parameter evaluation

An important question is which model parameters best explain the change in amyloid load between scans. With a two-tailed t-test, we see that the clearance parameter is significantly lower in subjects accumulating Aβ while the production parameter is not significantly different between visits. As has previously been shown, an increased production over clearance ratio is what drives the increase in Aβ load in symptomatic mutation carriers. This may further suggest that an impaired clearance system is the main contributor to increased Aβ load.

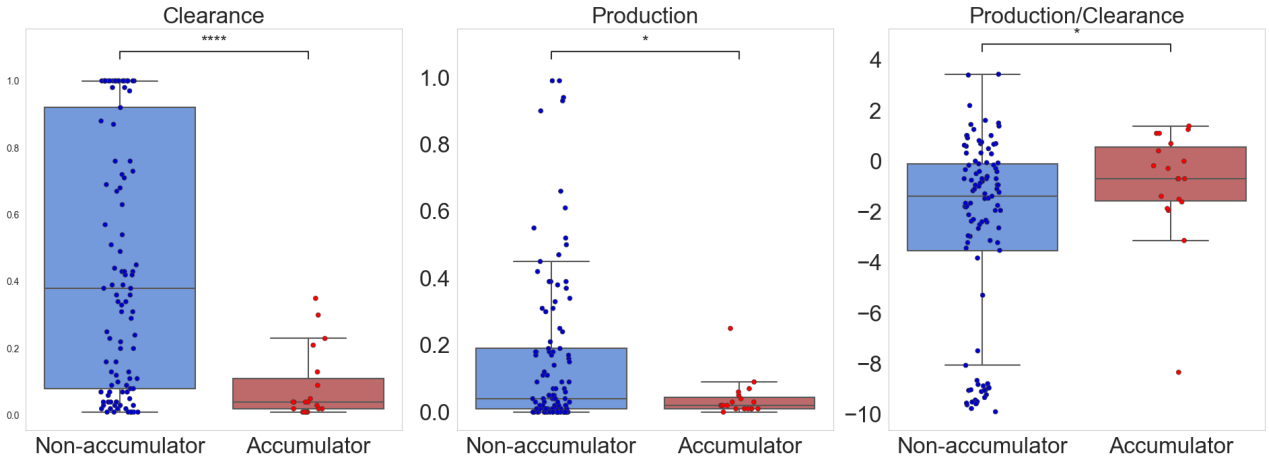

Figure 4.10: From left to right we show differences in the probabilistic production, clearance, and log-spaced production over clearance ratio for accumulators vs non-accumulators between timepoints 1 to 2. $0.01 < *p < 0.05$ $****p < 10^{-4}$

In Figure 4.11 we show the longitudinal ESM performances for an exemplar accumulator and non-accumulator across every production and clearance parameter value combination. It's evident that for both subjects, there is a separable space in which the ESM performs best, but the space spans more than one possible combination. This suggests that the parameters selected for each individual are not wholly interpretable, but that the overall parameter space for which the ESM performs best for a subject can be used to infer general trends. Indeed, the exemplar accumulator's best-performing space lies within the positive production/clearance ratio space whereas the non-accumulator's lies in the negative space. This may suggest that the nonaccumulator has a balanced production to clearance ratio or sufficiently high clearance of Aβ that hinders accumulation while the accumulator is not adequately clearing Aβ.

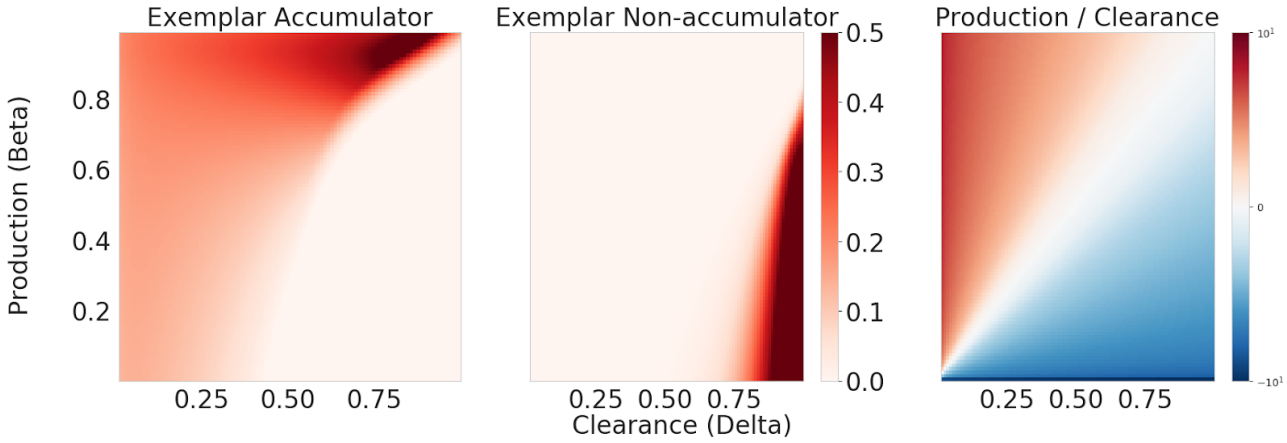

Figure 4.11: From left to right we show differences in the probabilistic production, clearance, and log-spaced production over clearance ratio for accumulators vs non-accumulators between timepoints 1 to 2. The arrows point to the production, clearance combinations that yield approximately equivalent ESM performance for a subject.

4.5 Longitudinal performance analysis

We sought to assess if parameters fit between subjects' first two timepoints can be used to predict the regional Aβ patterns at subjects' subsequent scans. Despite the better test-retest reliability observed when using the brainstem as the reference region, we found that the annual rates of accumulation for mean cortical Aβ probabilities were often variable between visits (Fig 4.12a). Due to this variability, parameters fit between the first two scans could not consistently explain the regional pattern of Aβ measured at a third scan, and the model performed best for those individuals for whom a consistently positive rate of change was observed. The average within subject performance was 11.9% (SD=22.3%). We observed that for subjects who did not accumulate Aβ between timepoints 1 and 2 but accumulated between timepoints 2 and 3, ESM underestimated the change observed between the second set of timepoints (NA-A). Similarly, ESM overestimated change for those subjects (A-NA) who accumulated between timepoints 1 and 2 but not between timepoints 2 and 3 (Fig 4.12c).

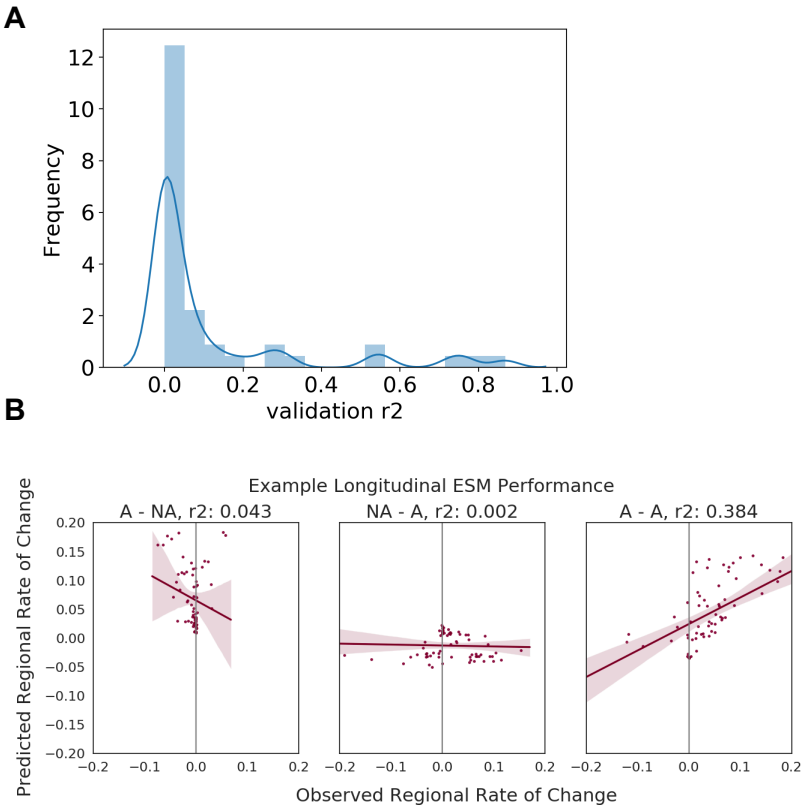

Figure 4.12: (a) Histogram of longitudinal validation performance across all subjects. (b) The observed and predicted regional rate of change between the 2nd and 3rd scan is shown for three example subjects in three categories, Accumulator-Nonaccumulator, Nonaccumulator-Accumulator, Accumulator-Accumulator across three visits.

Chapter 5

Discussion

With the advent of neuroimaging we have been better able to test hypotheses of Aβ spread in humans. While the trans-neuronal spread of misfolded proteins such as tau and α-synuclein has been supported by both studies in mice and humans, whether Aβ definitively spreads trans-neuronally as opposed to extracellulary is still contested. Throughout this thesis we have explored how well a model that simulates the trans-neuronal spread of Aβ under biologically feasible constraints of Aβ production and clearance can explain regional Aβ probabilities for subjects spanning the AD time-course. In this chapter we first discuss how using different PET preprocessing choices and connectivity measures affect the ESM's ability to reproduce cross-sectional data, followed by an exploration of how the ESM results can be interpreted in the context of the broader field of AD disease progression modelling. Lastly, we discuss the ESM's performance when used to predict future regional patterns of Aβ, limitations of the model, and recommendations for future work.

5.1 Effect of processing pipelines and connectivity measures on cross-sectional model performance

In our cross-sectional application of the ESM, we sought to evaluate how well the ESM performs across different PET processing pipelines, seed regions, and connectivity measures. A major difference between PUP and APPIAN is that PUP performs inter-frame motion correction and smoothing, and this may have contributed to the higher performance observed for ESM experiments which used data processed with PUP (Table 4.1). As discussed in Chapter 2.2.1.1, PET imaging is privy to a number of artifacts related to low spatial resolution and signal detection. Smoothing increases the signal to noise ratio at the expense of decreased resolution. Likewise,

inter-frame motion correction has been shown to be essential for sporadic AD studies where head motion frequently occurs and significantly impacts regional radiotracer binding quantification (Ikari et al., 2011). There is no gold standard for processing PET data in the context of familial AD, and previous work has reported that there are significant quantitative differences when using distinct reference regions (Su et al., 2019). In line with this study, we found that the reference region selection was most important for longitudinal analysis, as evidenced by the low test-retest reliability for the noncarriers of fAD mutations (Section 4.3.1).

5.1.1 Regional Aβ quantification

The processing choice that made the most substantial impact on model performance was the method used for computing Aβ deposition probabilities. As shown in Chapter 4 the method that yielded the best results was the voxelwise reference strategy introduced in the original ESM paper (V-ECDF-RR-EVD). The ESM assumes that network proximity governs regional levels of Aβ, so it follows that regions that are most proximal to the epicenter regions are expected to have the highest levels of Aβ. In Figure 4.4 we show that this is the case for the regional Aβ deposition probabilities and structural connectivity measure used for Model B. Compared with the other normalization methods we tested, this one is the most aggressive one with regard to how the null distribution is computed, suggesting that this method maximizes the signal to noise ratio.

5.1.2 Connectivity measures

Because structural and functional covariance patterns of healthy individuals have previously been shown to be associated with spatial patterns of AD, we simulated the spread of Aβ over both structural and functional connectivity matrices. As we can see in Figure 3.4, the structural connectivity matrix has stronger connections than the functional connectivity matrix, and are also more strongly correlated with the regional patterns of Aβ. ESM was able to explain the most variance in aggreggated Aβ patterns when fit over the structural connectome as opposed to the functional connectome. To test the hypothesis that Aβ spreads between brain regions that are spatially most proximal, we used a Euclidean distance matrix and found that the model was least successful using this measure of connectivity.

It is important to note that we did not exhaustively test every possible combination of preprocessing steps and measures of connectivity. With PUP we only used co-registered PET scans as we did not have access to parametric SUVR or DVR scans and subsequently could not use any of the voxelwise reference strategies to create Aβ

probabilites. The structural connectivity matrix we used is the same one used in the original application of the ESM, and the dataset used to create it is comprised of only 60 subjects. We could have additionally tested how the model would have performed using a structural connectivity matrix created using a much larger dataset such as the Human Connectome Project (HCP). With regard to functional connectivity, a recent preprint shed light on how processing of a single task-based fMRI dataset varied significantly across 70 labs (Botvinik-Nezer et al., 2019). There is no gold standard for processing rs-fMRI or DTI data, and the necessity of steps such as global signal regression and thresholding based on some amount of connectivity are contested. Future work could test how different post-processing steps impact the final functional connectivity matrix and ESM performance.

5.2 A deeper dive into the cross-sectional ESM results

Even with the best-performing models, Model A and B, we were only able to explain between 35-44% of the variance in aggregated regional Aβ patterns and on average, between 17-22% of the within subject patterns. This could be driven by multiple factors; in addition to the presence of measurement error, the model may not be a perfect descriptor of the underlying processes spurring the spatiotemporal spread of Aβ. Connectivity alone cannot perfectly explain the pattern as gene expression and molecular profiles of regions partly determine whether they will be vulnerable to Aβ accumulation. Using transcriptomic data from the Allen Brain atlas, Grothe et al showed that there is significant positive correlation between regional APP gene expression levels in cognitively normal subjects and those regions that typically exhibit Aβ accumulation in AD subjects. (Grothe et al., 2018). In a disease such as AD where two misfolded proteins, Aβ and tau, are at play and interact with one another, modelling one without taking into account the other may hinder our ability to fully explain the regional Aβ probabilities. For instance, when the ESM was used to model the spread of tau in the ADNI dataset, it was found that in regions where Aβ was present as well, tau probabilities were underestimated (Vogel et al., 2019). When applied cross-sectionally, the ESM is limited by its use of just one snapshot of a subject's disease trajectory to infer what happened prior to that scan. Specifically, it is argued a major drawback of using cross-sectional data is that it represents end-stage pathology; however, the DIAN dataset is unique in that it covers a much wider range of the disease timecourse, from more than 20 years before symptom onset to 20 years after symptom onset (Oxtoby and Alexander, 2017). Another drawback of cross-sectional data is that it is noisy, and incorporating group-level information could mitigate that issue. That being said, there are limitations to solely using group-level

information to model spatiotemporal changes as doing so requires disregarding the underlying heterogeneity of AD.

We note that the ESM did reproduce aggreggated regional Aβ patterns with more accuracy in the ADNI dataset than in the DIAN cohort (46% compared with 35-44%). One possible explanation is that the phenomena modelled by the ESM is happening to a larger extent in individuals spanning the AD spectrum for ADNI. However, it is difficult to definitively conclude that this is true given that the ADNI and DIAN PET data were also acquired using different radiotracers and were processed using different pipelines.

Ultimately, our results lend support to the hypothesis that Aβ propagates through neuronal connections. Keeping the aforementioned limitations in mind, we discuss the results of our statistical analysis comparing mechanisms driving Aβ propagation in fAD and sAD.

5.2.1 Seed regions

Although we did not test every region or combination of regions as the set of seed regions, we primarily were interested in learning if in fAD, neocortical regions can be used to reproduce the the baseline Aβ deposition pattern with high accuracy. In ADNI, the posterior cingulate and caudal anterior cingulate yielded the best results; however, we found that this was not the case for DIAN. The regions that yielded the highest performance were the medial orbitofrontal cortex, posterior cingulate, and precuneus. In fact, these regions were found to be the areas of earliest Aβ accumulation in sAD (Mattsson et al., 2019). Briefly - CSF and PET signal were used to stage subjects according to Aβ accumulation status, i.e. subjects who were both CSF and Aβ negative according to a set of data-driven thresholds were deemed to be nonaccumulators whereas those who were CSF positive but Aβ negative were deemed to be early Aβ accumulators. Regions pinpointed as areas of earliest accumulation were those that had significantly increased Aβ signal in early accumulators compared with non-accumulators. According to this system, the precuneus, medial orbitofrontal cortex, and posterior cingulate were all categorized as regions of early accumulation whereas the caudal anterior cingulate was pinpointed as an area of intermediate accumulation.

Because fAD mutation carriers have been repeatedly shown to have high Aβ signal in subcortical regions, particularly the caudate and putamen, we tested those out as well. Across all mutation types, we found that the performance was consistently higher using the aforementioned cortical epicenters, suggesting that while there may be high signal early on in the striatum, thalamus, and globus pallidus, the eventual spread of Aβ to other regions of the brain is most likely from the cortical epicenters.

5.2.2 Interpreting model parameters

It has long been hypothesized that the increased Aβ pathology in AD patients is caused by an imbalance of Aβ production and clearance - in particular, it has been assumed that in individuals with fAD mutations, this imbalance is driven by an over-production of the Aβ peptide. Being able to more definitively characterize the mechanism(s) via which Aβ pathology accumulates in those afflicted with sAD vs fAD was made possible with the development of the stable isotope labelling kinetics technique (SILK) which is a metabolic labeling technique that facilitates the measurement of real-time Aβ synthesis and clearance rates (Paterson et al., 2019). This technique has previously elucidated that sAD is characterized by reduced clearance of the Aβ-42 peptide while the production rate is not significantly different between controls (n=12) and sporadic AD patients (n=12) (Mawuenyega et al., 2010). In familial AD mutation carriers, the same team showed that Aβ accumulation is characterized by both over-production and reduced clearance in 11 mutation carriers compared with 12 controls (Potter et al., 2013).

In the present study, we use the results of a mathematical model to make inferences about the global processes of clearance and production. As such, within subject ESM performance dictates how strongly we can trust the model parameters. As discussed in Section 5.1, the performance of Model B was substantially negatively impacted by Aβ negativity. Unfortunately, due to the very small number of mutation carriers who could be classified as having late MCI or severe AD, we were limited to exploring parameter differences for a binary classification of asymptomatic vs symptomatic. Both global clearance and production rates were not significantly different between asymptomatic and symptomatic mutation carriers (Figure 4.5). Both clearance and production rates were quite low across all mutation carriers, and the low production rate can be attributed to a "saturation" effect where increasing sequestering of soluble Aβ agents into insoluble plaques, coupled with reduced clearance, results in a reduction of Aβ accumulation (Iturria-Medina et al., 2014).

Our results do not conclusively point to either Aβ over-production or under-clearance being significantly linked with cognitive symptomology or CSF levels of Aβ. Though a significant modulatory effect is observed for Aβ over-production on CSF Aβ, tau, and phosphorylated tau levels using ESM parameters gleaned from Model A, this effect is diluted when we look at only those individuals for whom the ESM was able to reproduce their regional Aβ patterns (Figure 4.6). The model parameters computed from the longitudinal application of the ESM suggest that short-term accumulation of Aβ may be linked to under-clearance, but the lack of significance of the original structural connectivity matrix undermines the certainty

with which we can make this assertion.

Ultimately, if we conclude that reduced Aβ clearance causes short-term accumulation of Aβ, the ESM's reduction of Aβ clearance to a single phenomenon hinders us from gaining further insight about the exact clearance mechanism(s). Multiple pathways for Aβ clearance from the brain exist: phagocytosis and endocytosis by various cell types including microglia, perivascular macrophages, astrocytes, oligendrocytes, and neurons; proteolytic degradation by enzymes; transportation across the BBB (Wang et al., 2017). Furthermore, Aβ exists in the peripheral nervous system as well, and effective clearance of Aβ from the brain has been linked to its clearance from the peripheral system in mice (Xiang et al., 2015). Thus, reduced clearance in AD can be driven by vascular dysregulation, impaired systemic or adaptive immunity, inflammation, and other systemic abnormalities. Immune therapy in the form of auto-antibodies that bind to specific antigens on Aβ aggreggates have been proposed a possible way to ameliorate reduced clearance in AD patients. Ultimately, what we are most interested in is whether targetting the reduced clearance of Aβ will also improve the cognitive symptoms characteristic of AD, and we would be remiss not to mention the latest news about Aducanumab, an anti-Aβ autoantibody, which has just been shown to improve CDR and MMSE scores in one cohort of older individuals with mild cognitive impairment in a phase 3 clinical trial("EMERGE and ENGAGE Topline Results: Two Phase 3 Studies to Evaluate Aducanumab in Patients With Early Alzheimer's Disease"). While this drug did not demonstrate the same effects of in a separate replication study, the limited success of Aducanumab lends support to the hypothesis that Aβ under-clearance is a more important target than Aβ over-production.

5.3 Utility of the ESM for making out of sample predictions

In addition to clarifying mechanistic similarities or differences between sAD and ADAD, in Aim 2 we sought to validate the ESM's predictive ability. Unfortunately, when we looked at the performance for the longitudinal ESM fitting across all subjects and regions, overall model performance was not significant with respect to whether the actual structural connectivity matrix or randomized connectivity matrices were used. Given the large degree of similarity between timepoints 1 and 2, it's possible that a simpler (more regularized) model would have higher performance. Two potential solutions to reduce model complexity would be for one joint production

over clearance ratio to be used and for the size of the connectivity matrix to be reduced to the more informative regions.

When we used model parameters fit between individuals' first two scans to predict the Aβ pattern at the third scan, we encountered the issue of variable rates of change for a given subject across multiple visits. This prevents the ESM from generalizing to future Aβ patterns as it expects a consistent rate of change.

5.4 Future work

Improvements to the current work can be made with respect to both the data-driven modelling and neuroimaging processing methods. To better compare the model results for ADNI and DIAN datasets, we can either use Florbetapir PET data for the DIAN dataset and ensure that the PET data of both cohorts are processed with exactly the same pipeline.

While discussing both the cross-sectional and longitudinal results, we've called for the integration of group-level information to make more stable predictions at an individual level. As was shown with Garbarino et al's ACP model (Garbarino, Lorenzi, and for the Alzheimer's Disease Neuroimaging Initiative, 2019), machine learning techniques such as Gaussian processes can be used to merge information from individuals across the disease time-course to make more informed predictions. The current implementation of the ACP makes the assumption that disease progression is homogenous for all individuals, but this can be addressed using unsupervised learning models that cluster individuals into subtypes. Group-level modelling could subsequently be done within these different subtypes.

5.5 Conclusion

5.5.1 Aim 1

1. The regional pattern of Aβ in both fAD and sAD is predominantly driven by white matter connectivity to an epicenter of Aβ accumulation.

2. The large dependence of cross-sectional model performance on data pre-processing should motivate future studies aimed at assessing the reproducibility of model performance across this and various other axes traditionally viewed as confounds.

3. We were unable to reproduce the significant relationship observed between Aβ clearance and clinical diagnosis in the ADNI dataset.

5.5.2 Aim 2

1. Our project is the first to validate ESM longitudinally.

2. The dynamic nature of Aβ progression hinders the ability of model parameters fit between two timepoints to consistently explain the regional pattern of Aβ observed at a future timepoint.

3. Future improvements to the ESM and other data-driven models of Aβ progression should incorporate genetic information about regional vulnerability, cross-sectional information to capture information along the full disease timecourse, and improved measures of connectivity.

Bibliography

Association, Alzheimer's (2018). "2018 Alzheimer's Disease Facts and Figures". In: *Alzheimer's & Dementia* 14.3, pp. 367–429. ISSN: 1552-5260. DOI: https://doi.org/10.1016/j.jalz.2018.02.001. URL: http://www.sciencedirect.com/science/article/pii/S1552526018300414.

Avants, Brian B. et al. (Dec. 2011). "An Open Source Multivariate Framework for N-Tissue Segmentation with Evaluation on Public Data". In: *Neuroinformatics* 9.4, pp. 381–400. ISSN: 1539-2791, 1559-0089. DOI: 10.1007/s12021-011-9109-y. URL: http://link.springer.com/10.1007/s12021-011-9109-y (visited on 11/07/2019).

Bateman, Randall J et al. (2010). "Autosomal-Dominant Alzheimer's Disease: A Review and Proposal for the Prevention of Alzheimer's Disease". In: *Alzheimer's Research & Therapy* 3.1, p. 1. ISSN: 1758-9193. DOI: 10.1186/alzrt59. URL: http://alzres.biomedcentral.com/articles/10.1186/alzrt59 (visited on 12/16/2019).

Bateman, Randall J. et al. (Aug. 30, 2012). "Clinical and Biomarker Changes in Dominantly Inherited Alzheimer's Disease". In: *New England Journal of Medicine* 367.9, pp. 795–804. ISSN: 0028-4793, 1533-4406. DOI: 10.1056/NEJMoa1202753. URL: http://www.nejm.org/doi/abs/10.1056/NEJMoa1202753 (visited on 07/05/2018).

Biogen. "EMERGE and ENGAGE Topline Results: Two Phase 3 Studies to Evaluate Aducanumab in Patients With Early Alzheimer's Disease". URL: https://investors.biogen.com/static-files/ddd45672-9c7e-4c99-8a06-3b557697c06f.

Botvinik-Nezer, Rotem et al. (Nov. 15, 2019). *Variability in the Analysis of a Single Neuroimaging Dataset by Many Teams*. preprint. Neuroscience. DOI: 10.1101/843193. URL: http://biorxiv.org/lookup/doi/10.1101/843193 (visited on 12/07/2019).

Brundin, Patrik, Ronald Melki, and Ron Kopito (Apr. 2010). "Prion-like Transmission of Protein Aggregates in Neurodegenerative Diseases". In: *Nature Reviews Molecular Cell Biology* 11.4, pp. 301–307. ISSN: 1471-0072, 1471-0080. DOI: 10.1038/nrm2873. URL: http://www.nature.com/articles/nrm2873 (visited on 11/18/2019).

Buckner, Randy L. et al. (2005). "Molecular, Structural, and Functional Characterization of Alzheimers Disease: Evidence for a Relationship between Default Activity, Amyloid, and Memory". In: *Journal of Neuroscience* 25.34, pp. 7709–7717. ISSN: 0270-6474. DOI: 10.1523/JNEUROSCI.2177-05.2005. eprint: https://www.jneurosci.org/content/25/34/7709.full.pdf. URL: https://www.jneurosci.org/content/25/34/7709.

Burns, Alistair and Steve Iliffe (Feb. 5, 2009). "Dementia". In: *BMJ* 338. ISSN: 0959-8138, 1468-5833. DOI: 10.1136/bmj.b75. pmid: 19196746. URL: https://www.bmj.com/content/338/bmj.b75 (visited on 11/18/2019).

Castellano, J. M. et al. (June 29, 2011). "Human apoE Isoforms Differentially Regulate Brain Amyloid-Peptide Clearance". In: *Science Translational Medicine* 3.89, 89ra57–89ra57. ISSN: 1946-6234, 1946-6242. DOI: 10.1126/scitranslmed.3002156. URL: http://stm.sciencemag.org/cgi/doi/10.1126/scitranslmed.3002156 (visited on 11/25/2019).

Chételat, Gaël et al. (2013). "Amyloid Imaging in Cognitively Normal Individuals, at-Risk Populations and Preclinical Alzheimer's Disease". In: *NeuroImage. Clinical* 2, pp. 356–365. ISSN: 2213-1582. DOI: 10.1016/j.nicl.2013.02.006. pmid: 24179789.

Cohen, Ann D. et al. (June 2018). "Early Striatal Amyloid Deposition Distinguishes Down Syndrome and Autosomal Dominant Alzheimer's Disease from Late-Onset Amyloid Deposition". In: *Alzheimer's & Dementia* 14.6, pp. 743–750. ISSN: 15525260. DOI: 10.1016/j.jalz.2018.01.002. URL: http://doi.wiley.com/10.1016/j.jalz.2018.01.002 (visited on 03/22/2020).

Collins, D. L. et al. (1994 Mar-Apr). "Automatic 3D Intersubject Registration of MR Volumetric Data in Standardized Talairach Space". In: *Journal of Computer Assisted Tomography* 18.2, pp. 192–205. ISSN: 0363-8715. pmid: 8126267.

Desikan, Rahul S. et al. (July 2006). "An Automated Labeling System for Subdividing the Human Cerebral Cortex on MRI Scans into Gyral Based Regions of Interest". In: *NeuroImage* 31.3, pp. 968–980. ISSN: 10538119. DOI: 10.1016/j.neuroimage.2006.01.021. URL: https://linkinghub.elsevier.com/retrieve/pii/S1053811906000437 (visited on 10/31/2019).

Eisele, Yvonne S. et al. (2009). "Induction of Cerebral B-Amyloidosis: Intracerebral versus Systemic AB Inoculation". In: *Proceedings of the National Academy of Sciences* 106.31, pp. 12926–12931. ISSN: 0027-8424. DOI: 10.1073/pnas.0903200106. eprint: https://www.pnas.org/content/106/31/12926.full.pdf. URL: https://www.pnas.org/content/106/31/12926.

Eskildsen, Simon F. et al. (Feb. 2012). "BEaST: Brain Extraction Based on Nonlocal Segmentation Technique". In: *NeuroImage* 59.3, pp. 2362–2373. ISSN: 10538119. DOI: 10.1016/j.neuroimage.2011.09.012. URL: https://linkinghub.elsevier.com/retrieve/pii/S1053811911010573 (visited on 11/07/2019).

Esteban, Oscar et al. (Sept. 2017). "MRIQC: Advancing the Automatic Prediction of Image Quality in MRI from Unseen Sites". In: *PLOS ONE* 12.9, pp. 1–21. DOI: 10.1371/journal.pone.0184661. URL: https://doi.org/10.1371/journal.pone.0184661.

Esteban, Oscar et al. (Jan. 2019). "fMRIPrep: A Robust Preprocessing Pipeline for Functional MRI". In: *Nature Methods* 16.1, pp. 111–116. ISSN: 1548-7091, 1548-7105. DOI: 10.1038/s41592-018-0235-4. URL: http://www.nature.com/articles/s41592-018-0235-4 (visited on 11/08/2019).

Fagan, A. M. et al. (Mar. 5, 2014). "Longitudinal Change in CSF Biomarkers in Autosomal-Dominant Alzheimer's Disease". In: *Science Translational Medicine* 6.226, 226ra30–226ra30. ISSN: 1946-6234, 1946-6242. DOI: 10.1126/scitranslmed.3007901. URL: http://stm.sciencemag.org/cgi/doi/10.1126/scitranslmed.3007901 (visited on 07/05/2018).

Fagan, Anne M. et al. (Apr. 2002). "Human and Murine ApoE Markedly Alters AB Metabolism before and after Plaque Formation in a Mouse Model of Alzheimer's Disease". In: *Neurobiology of Disease* 9.3, pp. 305–318. ISSN: 09699961. DOI: 10.1006/nbdi.2002.0483. URL: https://linkinghub.elsevier.com/retrieve/pii/S0969996102904833 (visited on 11/25/2019).

Frost, Bess and Marc I. Diamond (Mar. 2010). "Prion-like Mechanisms in Neurodegenerative Diseases". In: *Nature Reviews Neuroscience* 11.3, pp. 155–159. ISSN: 1471-003X, 1471-0048. DOI: 10.1038/nrn2786. URL: http://www.nature.com/articles/nrn2786 (visited on 11/18/2019).

Frost, Bess, Rachel L. Jacks, and Marc I. Diamond (May 8, 2009). "Propagation of Tau Misfolding from the Outside to the Inside of a Cell". In: *Journal of Biological Chemistry* 284.19, pp. 12845–12852. ISSN:

0021-9258, 1083-351X. DOI: 10.1074/jbc.M808759200. URL: http://www.jbc.org/lookup/doi/10.1074/jbc.M808759200 (visited on 11/25/2019).

Fujiwara, Ken et al. (May 1, 2016). "Which Parametric Images of PiB-PET Shows Superior Performance? : A Comparative Study among SUVR and DVR Images." In: *Journal of Nuclear Medicine* 57 (supplement 2), pp. 2633–2633. URL: http://jnm.snmjournals.org/content/57/supplement_2/2633.abstract.

Funck, Thomas et al. (Sept. 26, 2018). "APPIAN: Automated Pipeline for PET Image Analysis". In: *Frontiers in Neuroinformatics* 12, p. 64. ISSN: 1662-5196. DOI: 10.3389/fninf.2018.00064. URL: https://www.frontiersin.org/article/10.3389/fninf.2018.00064/full (visited on 11/07/2019).

Garbarino, Sara, Marco Lorenzi, and for the Alzheimer's Disease Neuroimaging Initiative (2019). "Modeling and Inference of Spatio-Temporal Protein Dynamics Across Brain Networks". In: *Information Processing in Medical Imaging*. Ed. by Albert C. S. Chung et al. Vol. 11492. Cham: Springer International Publishing, pp. 57–69. ISBN: 978-3-030-20350-4 978-3-030-20351-1. DOI: 10.1007/978-3-030-20351-1_5. URL: http://link.springer.com/10.1007/978-3-030-20351-1_5 (visited on 11/19/2019).

Gordon, Brian A et al. (Mar. 2018). "Spatial Patterns of Neuroimaging Biomarker Change in Individuals from Families with Autosomal Dominant Alzheimer's Disease: A Longitudinal Study". In: *The Lancet Neurology* 17.3, pp. 241–250. ISSN: 14744422. DOI: 10.1016/S1474-4422(18)30028-0. URL: https://linkinghub.elsevier.com/retrieve/pii/S1474442218300280 (visited on 10/25/2019).

Greicius, Michael D. et al. (2004). "Default-Mode Network Activity Distinguishes Alzheimers Disease from Healthy Aging: Evidence from Functional MRI". In: *Proceedings of the National Academy of Sciences* 101.13, pp. 4637–4642. ISSN: 0027-8424. DOI: 10.1073/pnas.0308627101. eprint: https://www.pnas.org/content/101/13/4637.full.pdf. URL: https://www.pnas.org/content/101/13/4637.

Grothe, Michel J. et al. (Nov. 14, 2017). "In Vivo Staging of Regional Amyloid Deposition". In: *Neurology* 89.20, pp. 2031–2038. ISSN: 0028-3878, 1526-632X. DOI: 10.1212/WNL.0000000000004643. URL: http://www.neurology.org/lookup/doi/10.1212/WNL.0000000000004643 (visited on 11/10/2019).

Grothe, Michel J et al. (July 16, 2018). "Molecular Properties Underlying Regional Vulnerability to Alzheimer's Disease Pathology". In: *Brain*. ISSN: 0006-8950, 1460-2156. DOI: 10.1093/brain/awy189. URL: https://academic.oup.com/brain/advance-article/doi/10.1093/brain/awy189/5054650 (visited on 12/06/2019).

Haass, C. et al. (May 1, 2012). "Trafficking and Proteolytic Processing of APP". In: *Cold Spring Harbor Perspectives in Medicine* 2.5, a006270–a006270. ISSN: 2157-1422. DOI: 10.1101/cshperspect.a006270. URL: http://perspectivesinmedicine.cshlp.org/lookup/doi/10.1101/cshperspect.a006270 (visited on 11/22/2019).

Haass, Christian (Feb. 11, 2004). "Take Five—BACE and the Gamma-Secretase Quartet Conduct Alzheimer's Amyloid B-Peptide Generation". In: *The EMBO Journal* 23.3, pp. 483–488. ISSN: 0261-4189, 1460-2075. DOI: 10.1038/sj.emboj.7600061. URL: http://emboj.embopress.org/cgi/doi/10.1038/sj.emboj.7600061 (visited on 11/22/2019).

Hallbeck, Martin, Sangeeta Nath, and Jan Marcusson (Dec. 2013). "Neuron-to-Neuron Transmission of Neurodegenerative Pathology". In: *The Neuroscientist* 19.6, pp. 560–566. ISSN: 1073-8584, 1089-4098. DOI: 10.1177/1073858413494270. URL: http://journals.sagepub.com/doi/10.1177/1073858413494270 (visited on 11/18/2019).

Hardy, J. (July 19, 2002). "The Amyloid Hypothesis of Alzheimer's Disease: Progress and Problems on the Road to Therapeutics". In: *Science* 297.5580, pp. 353–356. ISSN: 00368075, 10959203. DOI: 10.1126/science.1072994. URL: http://www.sciencemag.org/cgi/doi/10.1126/science.1072994 (visited on 11/21/2019).

Hsia, A. Y. et al. (Mar. 16, 1999). "Plaque-Independent Disruption of Neural Circuits in Alzheimer's Disease Mouse Models". In: *Proceedings of the National Academy of Sciences* 96.6, pp. 3228–3233. ISSN: 0027-8424, 1091-6490. DOI: 10.1073/pnas.96.6.3228. URL: http://www.pnas.org/cgi/doi/10.1073/pnas.96.6.3228 (visited on 11/18/2019).

Hudry, E. et al. (Nov. 20, 2013). "Gene Transfer of Human Apoe Isoforms Results in Differential Modulation of Amyloid Deposition and Neurotoxicity in Mouse Brain". In: *Science Translational Medicine* 5.212, 212ra161–212ra161. ISSN: 1946-6234, 1946-6242. DOI: 10.1126/scitranslmed.3007000. URL: http://stm.sciencemag.org/cgi/doi/10.1126/scitranslmed.3007000 (visited on 11/25/2019).

Iadecola, Costantino (May 2004). "Neurovascular Regulation in the Normal Brain and in Alzheimer's Disease". In: *Nature Reviews Neuroscience* 5.5, pp. 347–360. ISSN: 1471-003X, 1471-0048. DOI: 10.1038/nrn1387. URL: http://www.nature.com/articles/nrn1387 (visited on 12/16/2019).

Iadecola, Costantino (Nov. 2013). "The Pathobiology of Vascular Dementia". In: *Neuron* 80.4, pp. 844–866. ISSN: 08966273. DOI: 10.1016/j.neuron.2013.10.008. URL: https://linkinghub.elsevier.com/retrieve/pii/S0896627313009112 (visited on 12/16/2019).

Ikari, Yasuhiko et al. (May 1, 2011). "Head Motion Evaluation and Correction for PET Scans with 18F-FDG in the Japanese Alzheimer's Disease Neuroimaging Initiative (J-ADNI) Multi-Center Study". In: *Journal of Nuclear Medicine* 52 (supplement 1), pp. 2091–2091. URL: http://jnm.snmjournals.org/content/52/supplement_1/2091.abstract.

Iturria-Medina, Y. et al. (July 2007). "Characterizing Brain Anatomical Connections Using Diffusion Weighted MRI and Graph Theory". In: *NeuroImage* 36.3, pp. 645–660. ISSN: 10538119. DOI: 10.1016/j.neuroimage.2007.02.012. URL: https://linkinghub.elsevier.com/retrieve/pii/S105381190700105X (visited on 11/01/2019).

Iturria-Medina, Y. et al. (June 21, 2016). "Early Role of Vascular Dysregulation on Late-Onset Alzheimer's Disease Based on Multifactorial Data-Driven Analysis". In: *Nature Communications* 7, p. 11934. ISSN: 2041-1723. DOI: 10.1038/ncomms11934. URL: http://www.nature.com/doifinder/10.1038/ncomms11934 (visited on 07/05/2018).

Iturria-Medina, Yasser, Félix M. Carbonell, and Alan C. Evans (Oct. 2018). "Multimodal Imaging-Based Therapeutic Fingerprints for Optimizing Personalized Interventions: Application to Neurodegeneration". In: *NeuroImage* 179, pp. 40–50. ISSN: 10538119. DOI: 10.1016/j.neuroimage.2018.06.028. URL: https://linkinghub.elsevier.com/retrieve/pii/S1053811918305354 (visited on 07/05/2018).

Iturria-Medina, Yasser et al. (Nov. 20, 2014). "Epidemic Spreading Model to Characterize Misfolded Proteins Propagation in Aging and Associated Neurodegenerative Disorders". In: *PLoS Computational Biology* 10.11. Ed. by Olaf Sporns, e1003956. ISSN: 1553-7358. DOI: 10.1371/journal.pcbi.1003956. URL: http://dx.plos.org/10.1371/journal.pcbi.1003956 (visited on 07/05/2018).

Iturria-Medina, Yasser et al. (May 2017). "Multifactorial Causal Model of Brain (Dis)Organization and Therapeutic Intervention: Application to Alzheimer's Disease". In: *NeuroImage* 152, pp. 60–77. ISSN: 10538119. DOI: 10.1016/j.neuroimage.2017.02.058. URL: https://linkinghub.elsevier.com/retrieve/pii/S1053811917301684 (visited on 12/07/2019).

Jucker, Mathias and Lary C. Walker (Sept. 2013). "Self-Propagation of Pathogenic Protein Aggregates in Neurodegenerative Diseases". In: *Nature* 501.7465, pp. 45–51. ISSN: 0028-0836, 1476-4687. DOI:

10.1038/nature12481. URL: http://www.nature.com/articles/nature12481 (visited on 11/18/2019).

K., Karmen (Dec. 18, 2013). "Basic PET Data Analysis Techniques". In: *Positron Emission Tomography - Recent Developments in Instrumentation, Research and Clinical Oncological Practice*. Ed. by Sandro Misciagna. InTech. ISBN: 978-953-51-1213-6. DOI: 10.5772/57126. URL: http://www.intechopen.com/books/positron-emission-tomography-recent-developments-in-instrumentation-research-and-clinical-oncological-practice/basic-pet-data-analysis-techniques (visited on 12/13/2019).

Kane, Michael D. et al. (2000). "Evidence for Seeding of B-Amyloid by Intracerebral Infusion of Alzheimer Brain Extracts in B-Amyloid Precursor Protein-Transgenic Mice". In: *Journal of Neuroscience* 20.10, pp. 3606–3611. ISSN: 0270-6474. DOI: 10.1523/JNEUROSCI.20-10-03606.2000. eprint: https://www.jneurosci.org/content/20/10/3606.full.pdf. URL: https://www.jneurosci.org/content/20/10/3606.

Karran, Eric, Marc Mercken, and Bart De Strooper (Sept. 2011). "The Amyloid Cascade Hypothesis for Alzheimer's Disease: An Appraisal for the Development of Therapeutics". In: *Nature Reviews Drug Discovery* 10.9, pp. 698–712. ISSN: 1474-1776, 1474-1784. DOI: 10.1038/nrd3505. URL: http://www.nature.com/articles/nrd3505 (visited on 12/16/2019).

Klein, Arno and Jason Tourville (2012). "101 Labeled Brain Images and a Consistent Human Cortical Labeling Protocol". In: *Frontiers in Neuroscience* 6. ISSN: 1662-4548. DOI: 10.3389/fnins.2012.00171. URL: http://journal.frontiersin.org/article/10.3389/fnins.2012.00171/abstract (visited on 10/31/2019).

Klein, William L. (Dec. 27, 2012). "Synaptotoxic Amyloid-B Oligomers: A Molecular Basis for the Cause, Diagnosis, and Treatment of Alzheimer's Disease?" In: *Journal of Alzheimer's Disease* 33.s1. Ed. by George Perry et al., S49–S65. ISSN: 18758908, 13872877. DOI: 10.3233/JAD-2012-129039. URL: https://www.medra.org/servlet/aliasResolver?alias=iospress&doi=10.3233/JAD-2012-129039 (visited on 12/13/2019).

Knopman, D. S. et al. (Nov. 2003). "Neuropathology of Cognitively Normal Elderly". In: *Journal of Neuropathology and Experimental Neurology* 62.11, pp. 1087–1095. ISSN: 0022-3069. DOI: 10.1093/jnen/62.11.1087. pmid: 14656067.

Landau, S. M. et al. (July 2014). "Amyloid PET Imaging in Alzheimer's Disease: A Comparison of Three Radiotracers". In: *European Journal of Nuclear Medicine and Molecular Imaging* 41.7, pp. 1398–1407. ISSN: 1619-7070, 1619-7089. DOI: 10.1007/s00259-014-2753-3. URL: http://link.springer.com/10.1007/s00259-014-2753-3 (visited on 12/16/2019).

Logan, J. et al. (Sept. 1990). "Graphical Analysis of Reversible Radioligand Binding from Time-Activity Measurements Applied to [N-11C-Methyl]-(-)-Cocaine PET Studies in Human Subjects". In: *Journal of Cerebral Blood Flow and Metabolism: Official Journal of the International Society of Cerebral Blood Flow and Metabolism* 10.5, pp. 740–747. ISSN: 0271-678X. DOI: 10.1038/jcbfm.1990.127. pmid: 2384545.

Lopresti, Brian J. et al. (Dec. 1, 2005). "Simplified Quantification of Pittsburgh Compound B Amyloid Imaging PET Studies: A Comparative Analysis". In: *Journal of Nuclear Medicine* 46.12, pp. 1959–1972. URL: http://jnm.snmjournals.org/content/46/12/1959.abstract.

Mathis, Chester A., Brian J. Lopresti, and William E. Klunk (Oct. 2007). "Impact of Amyloid Imaging on Drug Development in Alzheimer's Disease". In: *Nuclear Medicine and Biology* 34.7, pp. 809–822. ISSN: 09698051. DOI: 10.1016/j.nucmedbio.2007.06.015. URL: https://linkinghub.elsevier.com/retrieve/pii/S0969805107001771 (visited on 12/16/2019).

Mattsson, Niklas et al. (July 17, 2019). "Staging B-Amyloid Pathology With Amyloid Positron Emission Tomography". In: *JAMA Neurology*. ISSN: 2168-6149. DOI: 10.1001/jamaneurol.2019.2214. URL: http://archneur.jamanetwork.com/article.aspx?doi=10.1001/jamaneurol.2019.2214 (visited on 10/25/2019).

Mawuenyega, K. G. et al. (Dec. 24, 2010). "Decreased Clearance of CNS -Amyloid in Alzheimer's Disease". In: *Science* 330.6012, pp. 1774–1774. ISSN: 0036-8075, 1095-9203. DOI: 10.1126/science.1197623. URL: http://www.sciencemag.org/cgi/doi/10.1126/science.1197623 (visited on 12/08/2019).

Mazziotta, J et al. (Aug. 29, 2001). "A Probabilistic Atlas and Reference System for the Human Brain: International Consortium for Brain Mapping (ICBM)." In: *Philosophical Transactions of the Royal Society of London. Series B* 356.1412, pp. 1293–1322. ISSN: 0962-8436. DOI: 10.1098/rstb.2001.0915. pmid: 11545704. URL: https://www.ncbi.nlm.nih.gov/pmc/articles/PMC1088516/ (visited on 11/07/2019).

McKhann, Guy M. et al. (2011). "The Diagnosis of Dementia Due to Alzheimer's Disease: Recommendations from the National Institute on Aging-Alzheimer's Association Workgroups on Diagnostic Guidelines for Alzheimer's Disease". In: *Alzheimer's & Dementia* 7.3, pp. 263–269. ISSN: 1552-5260. DOI: https://doi.org/10.1016/j.jalz.2011.03.005. URL: http://www.sciencedirect.com/science/article/pii/S1552526011001014.

Meltzer, C. C. et al. (July 1990). "Correction of PET Data for Partial Volume Effects in Human Cerebral Cortex by MR Imaging". In: *Journal of Computer Assisted Tomography* 14.4, pp. 561–570. ISSN: 0363-8715. DOI: 10.1097/00004728-199007000-00011. pmid: 2370355.

Meyer-Luehmann, Melanie et al. (2006). "Exogenous Induction of Cerebral B-Amyloidogenesis Is Governed by Agent and Host". In: *Science* 313.5794, pp. 1781–1784. ISSN: 0036-8075. DOI: 10.1126/science.1131864. eprint: https://science.sciencemag.org/content/313/5794/1781.full.pdf. URL: https://science.sciencemag.org/content/313/5794/1781.

Morris, John C. et al. (Jan. 2010). "*APOE* Predicts Amyloid-Beta but Not Tau Alzheimer Pathology in Cognitively Normal Aging". In: *Annals of Neurology* 67.1, pp. 122–131. ISSN: 03645134, 15318249. DOI: 10.1002/ana.21843. URL: http://doi.wiley.com/10.1002/ana.21843 (visited on 11/25/2019).

Mucke, Lennart et al. (2000). "High-Level Neuronal Expression of aB1–42 in Wild-Type Human Amyloid Protein Precursor Transgenic Mice: Synaptotoxicity without Plaque Formation". In: *Journal of Neuroscience* 20.11, pp. 4050–4058. ISSN: 0270-6474. DOI: 10.1523/JNEUROSCI.20-11-04050.2000. eprint: https://www.jneurosci.org/content/20/11/4050.full.pdf. URL: https://www.jneurosci.org/content/20/11/4050.

Musiek, Erik S and David M Holtzman (June 2015). "Three Dimensions of the Amyloid Hypothesis: Time, Space and 'Wingmen'". In: *Nature Neuroscience* 18.6, pp. 800–806. ISSN: 1097-6256, 1546-1726. DOI: 10.1038/nn.4018. URL: http://www.nature.com/articles/nn.4018 (visited on 11/25/2019).

Nath, S. et al. (June 27, 2012). "Spreading of Neurodegenerative Pathology via Neuron-to-Neuron Transmission of -Amyloid". In: *Journal of Neuroscience* 32.26, pp. 8767–8777. ISSN: 0270-6474, 1529-2401. DOI: 10.1523/JNEUROSCI.0615-12.2012. URL: http://www.jneurosci.org/cgi/doi/10.1523/JNEUROSCI.0615-12.2012 (visited on 11/18/2019).

Oxtoby, Neil P. and Daniel C. Alexander (Aug. 2017). "Imaging plus X: Multimodal Models of Neurodegenerative Disease". In: *Current Opinion in Neurology* 30.4, pp. 371–379. ISSN: 1350-7540. DOI: 10.1097/WCO.0000000000000460. URL: http://Insights.ovid.com/crossref?an=00019052-201708000-00002 (visited on 12/07/2019).

Oxtoby, Neil P et al. (May 1, 2018). "Data-Driven Models of Dominantly-Inherited Alzheimer's Disease Progression". In: *Brain* 141.5, pp. 1529–1544. ISSN: 0006-8950, 1460-2156. DOI: 10.1093/brain/awy050. URL: https://academic.oup.com/brain/article/141/5/1529/4951528 (visited on 07/05/2018).

Palmqvist, Sebastian et al. (Dec. 2017). "Earliest Accumulation of B-Amyloid Occurs within the Default-Mode Network and Concurrently Affects Brain Connectivity". In: *Nature Communications* 8.1, p. 1214. ISSN: 2041-1723. DOI: 10.1038/s41467-017-01150-x. URL: http://www.nature.com/articles/s41467-017-01150-x (visited on 12/13/2019).

Palop, Jorge J., Jeannie Chin, and Lennart Mucke (Oct. 2006). "A Network Dysfunction Perspective on Neurodegenerative Diseases". In: *Nature* 443.7113, pp. 768–773. ISSN: 0028-0836, 1476-4687. DOI: 10.1038/nature05289. URL: http://www.nature.com/articles/nature05289 (visited on 11/19/2019).

Paterson, Ross W. et al. (July 2019). "SILK Studies — Capturing the Turnover of Proteins Linked to Neurodegenerative Diseases". In: *Nature Reviews Neurology* 15.7, pp. 419–427. ISSN: 1759-4758, 1759-4766. DOI: 10.1038/s41582-019-0222-0. URL: http://www.nature.com/articles/s41582-019-0222-0 (visited on 12/08/2019).

Pooley, Robert A. (July 2005). "Fundamental Physics of MR Imaging". In: *RadioGraphics* 25.4, pp. 1087–1099. ISSN: 0271-5333, 1527-1323. DOI: 10.1148/rg.254055027. URL: http://pubs.rsna.org/doi/10.1148/rg.254055027 (visited on 12/16/2019).

Potter, R. et al. (June 12, 2013). "Increased in Vivo Amyloid- 42 Production, Exchange, and Loss in Presenilin Mutation Carriers". In: *Science Translational Medicine* 5.189, 189ra77–189ra77. ISSN: 1946-6234, 1946-6242. DOI: 10.1126/scitranslmed.3005615. URL: http://stm.sciencemag.org/cgi/doi/10.1126/scitranslmed.3005615 (visited on 12/08/2019).

Price, J. L. and J. C. Morris (Mar. 1999). "Tangles and Plaques in Nondemented Aging and "Preclinical" Alzheimer's Disease". In: *Annals of Neurology* 45.3, pp. 358–368. ISSN: 0364-5134. DOI: 10.1002/1531-8249(199903)45:3<358::aid-ana12>3.0.co;2-x. pmid: 10072051.

Raj, Ashish, Amy Kuceyeski, and Michael Weiner (2012). "A Network Diffusion Model of Disease Progression in Dementia". In: *Neuron* 73.6, pp. 1204–1215. ISSN: 0896-6273. DOI: https://doi.org/10.1016/j.neuron.2011.12.040. URL: http://www.sciencedirect.com/science/article/pii/S0896627312001353.

Raj, Ashish et al. (Jan. 2015). "Network Diffusion Model of Progression Predicts Longitudinal Patterns of Atrophy and Metabolism in Alzheimer's Disease". In: *Cell Reports* 10, pp. 359–369. DOI: 10.1016/j.celrep.2014.12.034. URL: http://linkinghub.elsevier.com/retrieve/pii/S2211124714010638 (visited on 07/05/2018).

Readnower, Ryan D., Andrew D. Sauerbeck, and Patrick G. Sullivan (2011). "Mitochondria, Amyloid B, and Alzheimer's Disease". In: *International Journal of Alzheimer's Disease* 2011, pp. 1–5. ISSN: 2090-0252. DOI: 10.4061/2011/104545. URL: http://www.hindawi.com/journals/ijad/2011/104545/ (visited on 12/15/2019).

Ries, Miriam and Magdalena Sastre (July 5, 2016). "Mechanisms of AB Clearance and Degradation by Glial Cells". In: *Frontiers in Aging Neuroscience* 8. ISSN: 1663-4365. DOI: 10.3389/fnagi.2016.00160. URL: http://journal.frontiersin.org/Article/10.3389/fnagi.2016.00160/abstract (visited on 11/20/2019).

Rius-Pérez, S. et al. (2018). "Vascular Pathology: Cause or Effect in Alzheimer Disease?" In: *Neurología (English Edition)* 33.2, pp. 112–120. ISSN: 2173-5808. DOI: https://doi.org/10.1016/j.nrleng.2015.07.008. URL: http://www.sciencedirect.com/science/article/pii/S2173580816301298.

Rousset, O. G., Y. Ma, and A. C. Evans (May 1998). "Correction for Partial Volume Effects in PET: Principle and Validation". In: *Journal of Nuclear Medicine: Official Publication, Society of Nuclear Medicine* 39.5, pp. 904–911. ISSN: 0161-5505. pmid: 9591599.

Seeley, William W. et al. (2009). "Neurodegenerative Diseases Target Large-Scale Human Brain Networks". In: *Neuron* 62.1, pp. 42–52. ISSN: 0896-6273. DOI: https://doi.org/10.1016/j.neuron.2009.03.024. URL: http://www.sciencedirect.com/science/article/pii/S0896627309002499.

Shah, Hiral et al. (2016). "Research Priorities to Reduce the Global Burden of Dementia by 2025". In: *The Lancet Neurology* 15.12, pp. 1285–1294. ISSN: 1474-4422. DOI: https://doi.org/10.1016/S1474-4422(16)30235-6. URL: http://www.sciencedirect.com/science/article/pii/S1474442216302356.

Shepherd, Claire, Heather McCann, and Glenda Margaret Halliday (July 2009). "Variations in the Neuropathology of Familial Alzheimer's Disease". In: *Acta Neuropathologica* 118.1, pp. 37–52. ISSN: 0001-6322, 1432-0533. DOI: 10.1007/s00401-009-0521-4. URL: http://link.springer.com/10.1007/s00401-009-0521-4 (visited on 11/25/2019).

Soares, José M. et al. (2013). "A Hitchhiker's Guide to Diffusion Tensor Imaging". In: *Frontiers in Neuroscience* 7, p. 31. ISSN: 1662-4548. DOI: 10.3389/fnins.2013.00031. pmid: 23486659.

Song, Ha-Lim et al. (2014). "B-Amyloid Is Transmitted via Neuronal Connections along Axonal Membranes". In: *Annals of Neurology* 75.1, pp. 88–97. ISSN: 1531-8249. DOI: 10.1002/ana.24029. URL: https://onlinelibrary.wiley.com/doi/abs/10.1002/ana.24029 (visited on 11/18/2019).

Su, Yi et al. (Nov. 6, 2013). "Quantitative Analysis of PiB-PET with FreeSurfer ROIs". In: *PLoS ONE* 8.11. Ed. by Kewei Chen, e73377. ISSN: 1932-6203. DOI: 10.1371/journal.pone.0073377. URL: http://dx.plos.org/10.1371/journal.pone.0073377 (visited on 10/30/2019).

Su, Yi et al. (Mar. 24, 2016). "Quantitative Amyloid Imaging in Autosomal Dominant Alzheimer's Disease: Results from the DIAN Study Group". In: *PLOS ONE* 11.3. Ed. by Karl Herholz, e0152082. ISSN: 1932-6203. DOI: 10.1371/journal.pone.0152082. URL: http://dx.plos.org/10.1371/journal.pone.0152082 (visited on 10/31/2019).

Su, Yi et al. (Dec. 2019). "Comparison of Pittsburgh Compound B and Florbetapir in Cross-Sectional and Longitudinal Studies". In: *Alzheimer's & Dementia: Diagnosis, Assessment & Disease Monitoring* 11, pp. 180–190. ISSN: 23528729. DOI: 10.1016/j.dadm.2018.12.008. URL: https://linkinghub.elsevier.com/retrieve/pii/S2352872918300903 (visited on 10/30/2019).

Tiraboschi, P. et al. (June 8, 2004). "The Importance of Neuritic Plaques and Tangles to the Development and Evolution of AD". In: *Neurology* 62.11, pp. 1984–1989. ISSN: 1526-632X. DOI: 10.1212/01.wnl.0000129697.01779.0a. pmid: 15184601.

Vemuri, Prashanthi et al. (2009). "Effect of APOE on Biomarkers of Amyloid Load and Neuronal Pathology in AD". In: *Annals of Neurology*, NA–NA. ISSN: 03645134, 15318249. DOI: 10.1002/ana.21953. URL: http://doi.wiley.com/10.1002/ana.21953 (visited on 11/25/2019).

Verghese, P. B. et al. (May 7, 2013). "ApoE Influences Amyloid- (A) Clearance despite Minimal apoE/A Association in Physiological Conditions". In: *Proceedings of the National Academy of Sciences* 110.19, E1807–E1816. ISSN: 0027-8424, 1091-6490. DOI: 10.1073/pnas.1220484110. URL: http://www.pnas.org/cgi/doi/10.1073/pnas.1220484110 (visited on 11/25/2019).

Villemagne, Victor L. et al. (Dec. 1, 2009). "High Striatal Amyloid B-Peptide Deposition Across Different Autosomal Alzheimer Disease Mutation Types". In: *Archives of Neurology* 66.12. ISSN: 0003-9942. DOI: 10.1001/archneurol.2009.285. URL: http://archneur.jamanetwork.com/article.aspx?doi=10.1001/archneurol.2009.285 (visited on 03/22/2020).

Villeneuve, Sylvia et al. (July 2015). "Existing Pittsburgh Compound-B Positron Emission Tomography Thresholds Are Too High: Statistical and Pathological Evaluation". In: *Brain* 138.7, pp. 2020–2033. ISSN: 0006-8950. DOI: 10.1093/brain/aww112. pmid: 25953778. URL: https://www.ncbi.nlm.nih.gov/pmc/articles/PMC4806716/ (visited on 11/10/2019).

Vogel, Jacob W. et al. (Feb. 20, 2019). *Spread of Pathological Tau Proteins through Communicating Neurons in Human Alzheimer's Disease*. preprint. Neuroscience. DOI: 10.1101/555821. URL: http://biorxiv.org/lookup/doi/10.1101/555821 (visited on 10/30/2019).

Walker, Lary C. and Harry LeVine (Sept. 28, 2012). "Corruption and Spread of Pathogenic Proteins in Neurodegenerative Diseases". In: *Journal of Biological Chemistry* 287.40, pp. 33109–33115. ISSN: 0021-9258, 1083-351X. DOI: 10.1074/jbc.R112.399378. URL: http://www.jbc.org/lookup/doi/10.1074/jbc.R112.399378 (visited on 11/25/2019).

Walker, Lary C et al. (2002). "Exogenous Induction of Cerebral B-Amyloidosis in B-APP-Transgenic Mice". In: *Peptides* 23.7, pp. 1241–1247. ISSN: 0196-9781. DOI: https://doi.org/10.1016/S0196-9781(02)00059-1. URL: http://www.sciencedirect.com/science/article/pii/S0196978102000591.

Walsh, Dominic M. and Dennis J. Selkoe (2007). "AB Oligomers – a Decade of Discovery". In: *Journal of Neurochemistry* 101.5, pp. 1172–1184. ISSN: 1471-4159. DOI: 10.1111/j.1471-4159.2006.04426.x. URL: https://onlinelibrary.wiley.com/doi/abs/10.1111/j.1471-4159.2006.04426.x (visited on 11/18/2019).

Wang, Jun et al. (Oct. 2017). "A Systemic View of Alzheimer Disease — Insights from Amyloid-B Metabolism beyond the Brain". In: *Nature Reviews Neurology* 13.10, pp. 612–623. ISSN: 1759-4758, 1759-4766. DOI: 10.1038/nrneurol.2017.111. URL: http://www.nature.com/articles/nrneurol.2017.111 (visited on 12/08/2019).

Waters, Jack (2010). "The Concentration of Soluble Extracellular Amyloid-b Protein in Acute Brain Slices from CRND8 Mice". In: *PLoS ONE* 5.12, p. 16.

Watts, Joel C. et al. (2011). "Bioluminescence Imaging of AB Deposition in Bigenic Mouse Models of Alzheimers Disease". In: *Proceedings of the National Academy of Sciences* 108.6, pp. 2528–2533. ISSN: 0027-8424. DOI: 10.1073/pnas.1019034108. eprint: https://www.pnas.org/content/108/6/2528.full.pdf. URL: https://www.pnas.org/content/108/6/2528.

Westerman, Marcus A. et al. (2002). "The Relationship between aB and Memory in the Tg2576 Mouse Model of Alzheimers Disease". In: *Journal of Neuroscience* 22.5, pp. 1858–1867. ISSN: 0270-6474. DOI: 10.1523/JNEUROSCI.22-05-01858.2002. eprint: https://www.jneurosci.org/content/22/5/1858.full.pdf. URL: https://www.jneurosci.org/content/22/5/1858.

Xiang, Yang et al. (Oct. 2015). "Physiological Amyloid-Beta Clearance in the Periphery and Its Therapeutic Potential for Alzheimer's Disease". In: *Acta Neuropathologica* 130.4, pp. 487–499. ISSN: 0001-6322, 1432-0533. DOI: 10.1007/s00401-015-1477-1. URL: http://link.springer.com/10.1007/s00401-015-1477-1 (visited on 12/08/2019).

Yeh, Fang-Cheng and Wen-Yih Isaac Tseng (Sept. 2011). "NTU-90: A High Angular Resolution Brain Atlas Constructed by q-Space Diffeomorphic Reconstruction". In: *NeuroImage* 58.1, pp. 91–99. ISSN: 10538119. DOI: 10.1016/j.neuroimage.2011.06.021. URL: https://linkinghub.elsevier.com/retrieve/pii/S1053811911006392 (visited on 11/01/2019).

Young, Alexandra et al. (Dec. 2018). "Uncovering the Heterogeneity and Temporal Complexity of Neurodegenerative Diseases with Subtype and Stage Inference". In: *Nature Communications* 9.1, p. 4273. ISSN: 2041-1723. DOI: 10.1038/s41467-018-05892-0. URL: http://www.nature.com/articles/s41467-018-05892-0 (visited on 11/21/2019).

Zhou, Juan et al. (2012). "Predicting Regional Neurodegeneration from the Healthy Brain Functional Connectome". In: *Neuron* 73.6, pp. 1216–1227. ISSN: 0896-6273. DOI: https://doi.org/10.1016/j.neuron.2012.03.004. URL: http://www.sciencedirect.com/science/article/pii/S0896627312002279.

Zlokovic, Berislav V. (Dec. 2011). "Neurovascular Pathways to Neurodegeneration in Alzheimer's Disease and Other Disorders". In: *Nature Reviews Neuroscience* 12.12, pp. 723–738. ISSN: 1471-003X, 1471-0048. DOI: 10.1038/nrn3114. URL: http://www.nature.com/articles/nrn3114 (visited on 12/16/2019).

Appendix A

Supplementary Section

A.1 Cerebellum vs Brainstem as Longitudinal Reference Region

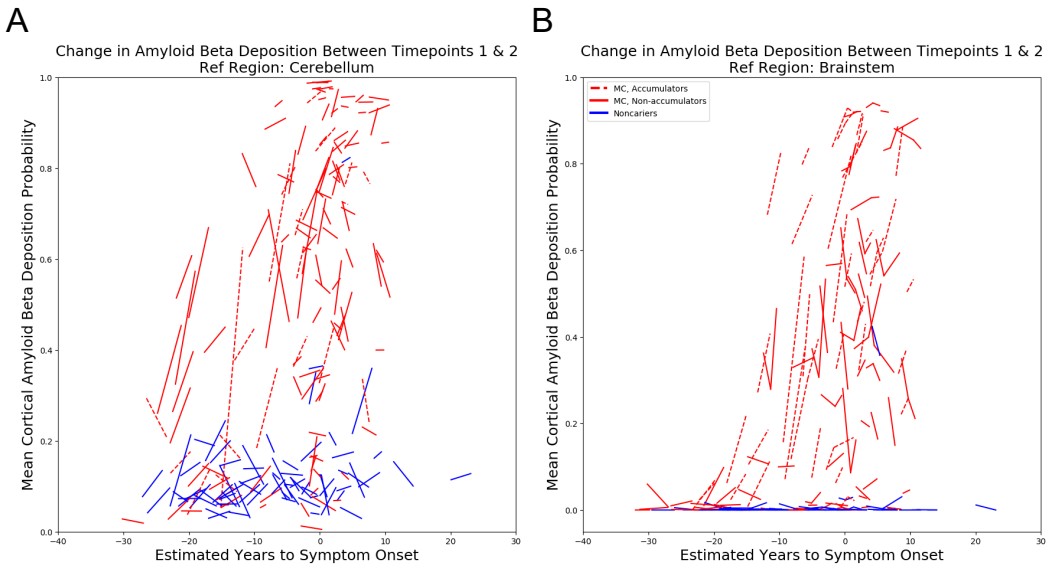

Figure A.1: On the left we show the average longitudinal changes for a set of cortical ROIs using the CC as the reference region. Noncarriers are in blue while mutation carriers are in red. On the right, we have the longitudinal changes using the brainstem as the epicenter. We note that the signal for the noncarriers' is much more stable using the brainstem as the reference region.